

THE SPECIFIC STAR FORMATION RATE AND STELLAR MASS FRACTION OF LOW-MASS CENTRAL GALAXIES IN COSMOLOGICAL SIMULATIONS

V. AVILA-REESE¹, P. COLÍN², A. GONZÁLEZ-SAMANIEGO¹, O. VALENZUELA¹, C. FIRMANI^{1,3}, H. VELÁZQUEZ⁴, AND D. CEVERINO⁵

Submitted

ABSTRACT

By means of cosmological N -body + Hydrodynamics simulations of galaxies in the context of the Λ Cold Dark Matter (Λ CDM) scenario we explore the specific star formation rates ($\text{SSFR} = \text{SFR}/M_s$, M_s is the stellar mass) and stellar mass fractions ($F_s \equiv M_s/M_h$, M_h is the halo mass) for sub- M^* field galaxies at different redshifts ($0 \lesssim z \lesssim 1.5$). Distinct low-mass halos ($2.5 \lesssim M_h/10^{10} M_\odot \lesssim 50$ at $z = 0$) were selected for the high-resolution re-simulations. The Hydrodynamics Adaptive Refinement Tree (ART) code was used and some variations of the sub-grid parameters were explored. Most simulated galaxies, specially those with the highest resolutions, have significant disk components and their structural and dynamical properties are in reasonable agreement with observations of sub- M^* field galaxies. However, the SSFRs are 5-10 times smaller than the averages of several (compiled and homogenized here) observational determinations for field blue/star-forming galaxies at $z < 0.3$ (at low masses, most observed field galaxies are actually blue/star-forming). This inconsistency seems to remain even at $z \sim 1 - 1.5$, although it is less drastic. The F_s of simulated galaxies increases with M_h as semi-empirical inferences show. However, the values of F_s at $z \approx 0$ are $\sim 5 - 10$ times larger in the simulations than in the inferences; these differences increases probably to larger factors at $z \sim 1 - 1.5$. The inconsistencies reported here imply that simulated low-mass galaxies ($0.2 \lesssim M_s/10^9 M_\odot \lesssim 30$ at $z = 0$) assembled their stellar masses much earlier than observations suggest. Our results confirm the predictions found by means of Λ CDM-based models of disk galaxy formation and evolution for isolated low-mass galaxies (Firmani & Avila-Reese 2010), and highlight that our understanding and implementation of astrophysics into simulations and models are still lacking vital ingredients.

Subject headings: cosmology:dark matter — galaxies:evolution — galaxies:formation — galaxies:haloes — methods: N -body simulations

1. INTRODUCTION

Based on the recent observational achievements, an empirical picture of stellar mass (M_s) assembly history of galaxies as a function of mass is emerging. Probably, the most remarkable aspect in this picture is the so-called ‘downsizing’ phenomenon. The term ‘downsizing’ was coined by Cowie et al. (1996) to describe the rapid decline with cosmic time of the maximum rest-frame K -band luminosity of galaxies undergoing active star formation (SF). Since then, as new observational inferences appeared, this term has been used to describe a number of trends of the galaxy population as a function of mass, most of them related actually to different astrophysical phenomena and galaxy evolutionary stages as discussed in Fontanot et al. (2009, see also Neistein et al. 2006; Santini et al. 2009).

From the most general point of view, the many downsizing manifestations can be separated into those that refer to the evolution (i) of massive galaxies, which today are on average red and passive (quenched SF), and (ii) of less massive galaxies, which today are on average blue and star forming. This separation seems to have an astrophysical root;

that is, it is not based on a merely methodological division. For example, Firmani & Avila-Reese (2010, hereafter FA10) have inferred the *average* M_s growth tracks of galaxies as a function of mass (the ‘galaxian hybrid evolutionary tracks’, GHETs) by means of a semi-empirical approach, and showed that at each epoch there is a characteristic mass that separates galaxies into two populations. Galaxies more massive than $M_s(z=0) \approx 3 \times 10^{10} M_\odot$ are on average passive (their SSFRs have dramatically diminished, where $\text{SSFR} = \text{SFR}/M_s$ is the specific SF rate), besides the more massive is the galaxy, the earlier it transited from the active (blue, star-forming) to the passive (red, quenched) population (‘population downsizing’). Galaxies less massive than $M_s(z=0) \approx 3 \times 10^{10} M_\odot$ are on average yet blue and active, and the less massive the galaxy, the higher its SSFR and/or the faster its late M_s growth (‘downsizing in SSFR’). We recall that these are just average trends. In fact, there are other factors besides mass that intervene in the stellar mass build-up of galaxies, e.g., the large-scale environment in which galaxies evolve (e.g., Peng et al. 2010, and more references therein) and whether they are central or satellites objects (for a recent review see Weinmann et al. 2011).

A large amount of *direct look-back time* observations support the mentioned two downsizing phenomena:

- *For high-mass galaxies*, those with $M_s \gtrsim M^*$, where M^* is the characteristic mass of the stellar mass function ($\approx 10^{10.8} M_\odot$ at $z \sim 0$), observations show the existence of a decreasing with cosmic time characteristic mass at which the SFR is dramatically quenched or at which the stellar mass functions of early- and late-type galaxies cross, evidencing this a mass-dependent

¹ Instituto de Astronomía, Universidad Nacional Autónoma de México, A.P. 70-264, 04510, México, D.F., México

² Centro de Radioastronomía y Astrofísica, Universidad Nacional Autónoma de México, A.P. 72-3 (Xangari), Morelia, Michoacán 58089, México

³ INAF-Osservatorio Astronomico di Brera, via E.Bianchi 46, I-23807 Merate, Italy

⁴ Instituto de Astronomía, Universidad Nacional Autónoma de México, A.P. 877, Ensenada BC 22800, México

⁵ Racah Institute of Physics, The Hebrew University, Jerusalem 91904, Israel

migration from blue to red population (e.g., Bell et al. 2003, 2007; Bundy et al. 2006; Hopkins et al. 2007; Drory & Alvarez 2008; Vergani et al. 2008; Pozzetti et al. 2010).

- *For low-mass galaxies* ($M_s \ll M^*$, they are mostly late-type, star-forming systems), at least up to $z \sim 1 - 2$, and by using different SFR tracers and methods to estimate M_s , it was found that their SSFRs are surprisingly high even at $z \sim 0$ and, on average, the lower the mass, the higher the SSFR (e.g., Baldry et al. 2004; Bauer et al. 2005; Feulner et al. 2005; Zheng et al. 2007; Noeske et al. 2007b; Bell et al. 2007; Elbaz et al. 2007; Salim et al. 2007; Chen et al. 2009; Damen et al. 2009a,b; Santini et al. 2009; Oliver et al. 2010; Rodighiero et al. 2010; Karim et al. 2011).

1.1. Confronting the empirical picture to theoretical predictions

The current paradigm of galaxy formation and evolution is based on the hierarchical clustering scenario (White & Rees 1978; White & Frenk 1991) within the context of the Λ Cold Dark Matter (Λ CDM) cosmology. According to this scenario, galaxies form and evolve in the centres of hierarchically growing Λ CDM halos. Though at first glance contradictory, it was shown that the ‘population (or archaeological) downsizing’ related to massive galaxies has, at least partially, its natural roots in the hierarchical clustering process of the dark-matter halos and their progenitors distribution (Neistein et al. 2006, see also Guo & White 2008; Li, Mo & Gao 2008; Kereš et al. 2009). Besides, red massive galaxies are expected to have been formed in early collapsed massive (associated to high peak and clustered) halos that afterwards become part of groups and clusters of galaxies, leaving truncated therefore the mass growth of the galaxies associated to these halos. On the other hand, massive galaxies typically hosted in the past active galactic nuclei (AGN). The strong feedback of the AGN may help to stop gas accretion, truncating further the galaxy stellar growth and giving rise to shorter formation time-scales for more massive galaxies (Bower et al. 2006; Croton et al. 2006; De Lucia et al. 2006).

All the factors mentioned above work in the direction of reproducing the downsizing manifestations of massive galaxies within the hierarchical Λ CDM scenario (Fontanot et al. 2009) –though several questions remain yet open.

What about the downsizing related to low-mass galaxies? As discussed in Firmani et al. (2010) and FA10, disk galaxy evolutionary models in the context of the hierarchical Λ CDM scenario seem to face difficulties in reproducing both the high empirically determined values of SSFR and the SSFR downsizing trend of low-mass galaxies ($M_s \lesssim 3 \times 10^{10} M_\odot \ll M^*$), which are mainly blue/star-forming systems of disk-like morphology.

The gas infall rate onto the (model) disks is primarily driven by the cosmological halo mass aggregation history (Firmani & Avila-Reese 2000; van den Bosch 2000; Stringer & Benson 2007; Dutton & van den Bosch 2009; Firmani et al. 2010; Dutton et al. 2010a), which is hierarchical, i.e. the less massive the halo, the earlier its fast mass aggregation rate phase. The gas infall rate is the main driver of disk SFR (other factors related to the process of gas conversion into stars, local feedback, interstellar medium turbulence, etc. introduce minor systematic deviations). The large-scale

feedback over the gas exerted mainly by SNe explosions, may strongly affect the SFR history of low-mass disks mainly because it alters the primary gas infall rate. The SN feedback has been commonly invoked in semi-analytical models (SAM) to reproduce the faint-end flattening of the galaxy luminosity (or M_s) function, assuming that this feedback produces gas reheating and galactic outflows (see e.g., Benson et al. 2003, and more references therein). Firmani et al. (2010) experimented with different models of SN-driven galactic outflows (e.g., based on energy and momentum conservation) besides of the disk gas turbulence input due to SN feedback. They have found that the present-day stellar and baryonic mass fractions ($F_s \equiv M_s/M_h$ and $F_b \equiv M_b/M_h$, where M_h is the total -virial- halo mass and $M_b = M_s + M_g$, M_g is the galaxy cold gas mass) of low-mass galaxies can be roughly reproduced when assuming extreme (probably unrealistic) galactic outflow efficiencies (see also Dutton & van den Bosch 2009; Dutton et al. 2010a). However, in any model with galactic outflows it was possible to alter the SFR histories of their disk galaxies in order to reproduce the observed (at least up to $z \sim 1$) downsizing in SSFR and the too high SSFRs measured for small central galaxies at late epochs.

Firmani et al. (2010) experimented also with the possibility of late re-accretion of the ejected gas (in previous works it was assumed that the feedback-driven outflows eject gas from the small halos forever, but see e.g., Springel et al. 2001; De Lucia et al. 2004; Bertone et al. 2007; Oppenheimer & Davé 2008; Oppenheimer et al. 2010). For reasonable schemes of gas re-accretion as a function of halo mass, Firmani et al. (2010) found that the SSFR of galaxies increases but it does it in the opposite direction of the downsizing trend: the increase is larger for the more massive galaxies.

A related issue of Λ CDM-based low-mass (disk) galaxy models appears in the evolution of the M_s – M_h (or F_s – M_h) relation. The semi-empirical inferences of this relation (see e.g., Conroy & Wechsler 2009; Moster et al. 2010; Wang & Jing 2010; Behroozi et al. 2010) show that for a fixed value of M_h , F_s is not only very small at $z = 0$, but it becomes smaller at higher z . The Λ CDM-based disk galaxy evolutionary models predict the opposite, i.e. higher values of F_s at higher z for a fixed value of M_h (FA10).

The inconsistency between models and observations related to the stellar mass build-up of sub- M^* disk galaxies found in Firmani et al. (2010) and FA10 is connected with some issues reported in recent SAMs. In these works, based also on the hierarchical Λ CDM scenario, it was showed that the stellar population of small (both central and satellite) galaxies ($M_s \approx 10^{9.0} - 10^{10.5} M_\odot$) is assembled too early, becoming these galaxies older, redder, and with lower SSFRs at later epochs than the observed galaxies in the same mass range (Somerville et al. 2008; Fontanot et al. 2009; Santini et al. 2009; Pasquali et al. 2010; Liu et al. 2010). By means of a disk galaxy evolutionary model similar to FA10, Dutton et al. (2010a) found also that the SSFR of low-mass galaxies is below the average of that given by observations, specially at $z \sim 1 - 2$, though these authors conclude that their models roughly reproduce the main features of the observed SFR sequence.

1.2. Cosmological simulations of galaxy evolution

Due to the high non-linearity implied in the problem of halo/galaxy formation and evolution, cosmological N-body/hydrodynamical simulations offer the fairest way to at-

tain a realistic modeling of galaxies. However, this method is hampered by the large –currently unreachable– dynamic range required to model galaxy formation and evolution in the cosmological context, as well as by the complexity of the processes involved, mainly gas thermo-hydrodynamics and SF and its feedback on the surrounding medium. The latter processes occur at scales ($\lesssim 1 - 50$ pc) commonly below the accessible resolution in simulations. Therefore, “sub-grid” schemes based on physical models for these processes should be introduced in the codes.

In the last years, cosmological simulations have matured enough as to produce individual galaxies that at $z \sim 0$ look quite realistic (e.g., Governato et al. 2007, 2010; Naab et al. 2007; Mayer et al. 2008; Zavala et al. 2008; Ceverino & Klypin 2009; Gibson et al. 2009; Scannapieco et al. 2008; Piontek & Steinmetz 2011; Colín et al. 2010; Sawala et al. 2011; Agertz et al. 2011), though this success in most cases is conditioned by the assumed sub-grid schemes and parameters, and the resolution that limits the simulations to small boxes, where only one or a few galaxies are followed.

What do current cosmological N-body/hydrodynamical simulations of low-mass galaxies predict regarding their SSFR and F_s evolution? By using the Adaptive Refinement Tree code (ART Kravtsov et al. 1997) with hydrodynamics included (Kravtsov 2003), Colín et al. (2010, hereafter C10) have explored different SF schemes and sub-grid parameters for one simulated low-mass galaxy ($M_h \approx 7 \times 10^{10} M_\odot$ at $z = 0$) that develops a significant disk. For some cases, the obtained galaxy did not look like realistic. For other cases, several global dynamical, structural, and ISM properties of observed small galaxies were reproduced. However, even in these cases the SSFR and F_s at different z are respectively much lower and higher than the observational inferences, an issue that apparently would also share other simulations presented in the literature.

In this paper, our aim is *to measure at different epochs the SSFRs and stellar mass fractions (F_s) of sub- M^* central galaxies covering a large range of masses* obtained in state-of-the-art N-body/hydrodynamical cosmological simulations, and explore whether the mentioned-above issues of Λ CDM-based galaxy evolutionary models (as well as SAMs) are also present or not in the simulations. Here we will use the Hydrodynamics ART code with some of the most reliable sub-grid schemes/parameters explored in C10 and covering almost two orders of magnitude in M_s . The effects of resolution over the SSFR and F_s at different epochs will be also explored.

The plan of the paper is as follows. The code and the SF/feedback prescriptions used for the simulations are described in §2. In this section, the cosmological simulation and the different runs varying the SF/feedback parameters are also presented. In §3.1 some generalities of the simulated galaxies are discussed, while in §3.2 the SSFRs and F_s of all the simulations at $z = 0.00, 0.33, 1.00$, and 1.50 vs mass are presented and compared with several observational inferences. In §§4.1 we discuss the numerical results from previous works, and in §§4.2 the caveats of the observational determinations used here are discussed. Our conclusions are presented in §5.

2. THE SIMULATIONS

2.1. The Code

The numerical simulations used in this work were performed using the Hydrodynamics + N-body ART code

(Kravtsov et al. 1997; Kravtsov 2003). Among the physical processes included in ART are the cooling of the gas and its subsequent conversion into stars, thermal stellar feedback, self-consistent advection of metals, a UV heating background source.

The cooling and heating rates incorporate Compton heating/cooling, atomic, and *molecular Hydrogen and metal-lines* cooling, UV heating from a cosmological background radiation (Haardt & Madau 1996), and are tabulated for a temperature range of $10^2 < T < 10^9$ K and a grid of densities, metallicities, and redshifts using the CLOUDY code (Ferland et al. 1998, version 96b4).

Star formation is modeled as taking place in the coldest and densest collapsed regions, defined by $T < T_{\text{SF}}$ and $n_g > n_{\text{SF}}$, where T and n_g are the temperature and number density of the gas, respectively, and T_{SF} and n_{SF} are a temperature and density SF threshold. A stellar particle of mass m_* is placed in a grid cell where these conditions are simultaneously satisfied, and this mass is removed from the gas mass in the cell. The particle subsequently follows N-body dynamics. No other criteria are imposed. In most of the simulations presented here, the stellar particle mass, m_* , is calculated by assuming that a given fraction (SF local efficiency factor ϵ_{SF}) of the cell gas mass, m_g , is converted into stars; that is, $m_* = \epsilon_{\text{SF}} m_g$, where ϵ_{SF} is treated as a free parameter. Based on the simulations performed in C10, where actually ϵ_{SF} was not a fixed parameter but a quantity calculated in each cell and timestep by an algorithm dependent on other parameters, we have found that when ϵ_{SF} acquires values around 0.5, the simulation gives reasonable results. This value is high enough for the thermal feedback to be efficient in regions of dense, cold, star-forming gas and not as large as to imply that most of the cell gas is exhausted.

In C10, besides the “deterministic” SF prescription described above, the authors experimented also with a “stochastic” or “random” SF prescription in which stellar particles are created in a cell with a probability function proportional to the gas density. The stochastic prescription allows for the possibility (with low probability) of forming stars in regions of low average density, in which isolated dense clouds are not resolved. Here, all of our simulations, except one, use the “deterministic” SF prescription assuming a density threshold of $n_{\text{SF}} = 6 \text{ cm}^{-3}$, which corresponds to a gas column density $N \sim 10^{21} \text{ cm}^{-2}$ (roughly the lower limit of observed giant molecular clouds) in a cell of $100 - 150$ pc (see C10).

Since stellar particle masses are much more massive than the mass of a star, typically $10^4 - 10^5 M_\odot$, once formed, each stellar particle is considered as a single stellar population, within which the individual stellar masses are distributed according to the Miller & Scalo IMF. Stellar particles eject metals and thermal energy through stellar winds and type II and Ia supernovae (SNe) explosions. Each star more massive than $8 M_\odot$ is assumed to dump into the ISM, instantaneously, 2×10^{51} ergs in the form of *thermal energy*; 10^{51} ergs comes from the stellar wind, and the other 10^{51} ergs from the SN explosion. Moreover, the star is assumed to eject $1.3 M_\odot$ of metals. For the assumed Miller & Scalo (1979) initial mass function, IMF, a stellar particle of $10^5 M_\odot$ produces 749 type II SNe. For a more detailed discussion of the processes implemented in the code, see Kravtsov (2003) and Kravtsov et al. (2005).

Stellar particles dump energy in the form of heat to the cells in which they are born. Most of this thermal energy, inside the cell, is radiated away unless the cooling is turned off tem-

porally. This mechanism along with a relatively high value of ϵ_{SF} allow the gas to expand and move away from the star forming region. Thus, to allow for outflows, in the present paper we adopt the strategy of turning off the cooling during a time t_{off} in the cells where stellar particles form (see C10). As t_{off} can be linked to the crossing time in the cell at the finest grid, we could see this parameter as depending on resolution in the sense that the higher the resolution, the smaller its value. In most simulations presented in this work, we turn off the cooling for $t_{\text{off}} = 40, 20$, and 10 Myr depending on resolution; however, we have found that varying this time, within this range, for a given simulation, does not affect significantly the results.

2.2. Numerical strategy and the runs

Most simulations presented here were run in a Λ CDM cosmology with $\Omega_0 = 0.3$, $\Omega_\Lambda = 0.7$, $\Omega_b = 0.045$, and $h = 0.7$. The CDM power spectrum is taken from Klypin & Holtzman (1997) and it is normalized to $\sigma_8 = 0.8$, where σ_8 is the rms amplitude of mass fluctuations in $8 h^{-1}\text{Mpc}$ spheres. Few simulations were run using a different cosmological set up (models C, F, and H of Table 1). For them, $\Omega_0 = 0.27$, $\Omega_\Lambda = 0.73$, $\Omega_b = 0.047$, and $h = 0.7$, and the power spectrum is that one used to run the “Bolshoi simulation” (Klypin et al. 2010) with $\sigma_8 = 0.82$.

To maximize resolution efficiency, we use the “zoom-in” technique. First a low-resolution cosmological simulations with only dark matter (DM) particles is run, and then regions (DM halos) of interest are picked up to be re-simulated with high resolution and with the physics of the gas included. The low-resolution simulations were run with 128^3 particles inside a box of $10h^{-1}\text{Mpc}$ per side, with the box initially covered by a mesh of 128^3 cells (zero-th level cells). At $z = 0$, we search for low-mass halos ($2 \times 10^{10} \lesssim M_h/h^{-1}\text{M}_\odot \lesssim 4 \times 10^{11}$) that are not contained within larger halos (*distinct* halos), but the selection was not based on their MAHs.

Out of ten halos, seven do not have companion halos at $z = 0$ with a mass greater than 0.2 the mass of the selected halo within a distance $\lesssim 0.5h^{-1}\text{Mpc}$. On the other hand, two of them are $220 h^{-1}\text{kpc}$ away from each other (halos G and J , see Table 1), and finally, there is one halo (D) that is separated by $330 h^{-1}\text{kpc}$ from a halo with a mass of about 0.5 the mass of halo D .

A Lagrangian region of 2 or $3R_{\text{vir}}$ is identified at $z = 50$ and re-sampled with additional small-scale modes (Klypin et al. 2001). The virial radius, R_{vir} , is defined as the radius that encloses a mean density equal to Δ_{vir} times the mean density of the universe, where Δ_{vir} is a quantity that depends on Ω_0 , Ω_Λ and z . For example, for our cosmology $\Delta_{\text{vir}}(z = 0) = 338$ and $\Delta_{\text{vir}}(z = 1) = 203$. The number of DM particles in the high-resolution region depends on the number of DM species and the mass of the halo, but for models with four species (high-resolution) this vary from \sim half a million (model Ah) to about 4.7 million (model Ih), the least massive and the second most massive halos, respectively. The corresponding dark matter mass per particle of model galaxies (m_{dm}) is given in Table 1.

In ART, the initially uniform grid is refined recursively as the matter distribution evolves. The criterion chosen for refinement is based on gas or DM densities. The cell is refined when the mass in DM particles exceeds $1.3(1 - F_{b,U})m_p$ or the mass in gas is higher than $13.0F_{b,U}m_p$, where $m_p = m_{\text{dm}} + m_g = m_{\text{dm}}/(1 - F_{b,U})$ and $F_{b,U}$ is the universal baryon fraction, $F_{b,U} = 0.15$ for the cosmology used here; it

TABLE 1
PARAMETERS OF THE SIMULATIONS

Name	$M_h(z=0)$ (10^{10} M_\odot)	m_{dm} (10^4 M_\odot)	ℓ_{max} (pc)	ϵ_{SF}	t_{off} (10^6 yr)
A_{h1}	1.97	9.41	109	0.5	20
A_{h1}^*	2.01	9.41	109	0.5	20
B_{h1}	2.32	9.41	109	0.5	20
B_{h1}^*	2.46	9.41	109	0.5	20
C_{l1}	2.80	65.7	218	0.5	20
C_{h1}	2.48	8.28	109	0.5	20
C_{h1}^*	2.84	8.28	109	0.5	20
D_{h1}	3.65	9.40	109	0.5	20
E_{l1}	5.94	76.0	218	0.5	40
E_{h1}	5.11	9.40	109	0.5	10
E_{h2}	5.31	9.40	109	0.5	40
E_{h3}	5.76	9.40	109	0.2	40
F_{l1}	7.79	65.7	218	0.5	20
F_{h1}	6.56	8.28	109	0.5	20
G_{l1}	8.37	76.0	218	0.66	40
G_{l2}	9.52	76.0	218	—	40
H_{l1}	14.5	46.5	218	stoch. ^a	r.a. ^b
I_{l1}	30.4	76.0	218	0.5	40
I_{h1}	30.5	9.40	109	0.5	40
J_{l1}	35.8	76.0	218	0.66	40
J_{l2}	40.4	76.0	218	—	40

^aStochastic SF scheme

^b“Run away” model, without turning off cooling

is assumed that the mean DM and gas densities in the box are the corresponding universal averages. For the simulations presented in this paper, using multiple DM particle masses, the grid is always unconditionally refined to the third level (fourth level), corresponding to an effective grid size of 512^3 (1024^3). On the other hand, the maximum allowed refinement level was set to 9 and 10, for low and high resolution simulations, respectively. This implies spatial sizes of the finest grid cells of $\ell_{\text{max}} = 218$ and 109 comoving pc, respectively.

We have re-simulated, as described, the evolution of ten individual galaxy/halo systems covering a total halo mass (baryon + dark matter) range from $M_h \approx 2 \times 10^{10} \text{ M}_\odot$ to $M_h \approx 4 \times 10^{11} \text{ M}_\odot$ at $z = 0$. For most of these systems, we have run two or more simulations by varying the resolution, the SF local efficiency parameter ϵ_{SF} , the time during which cooling time (after SF events) is kept off, t_{off} , and, in one case, the SF scheme. Table 1 summarizes the characteristics of all the simulations studied here.

The first column gives the name of the run, denoted by a capital letter that refers to a particular galaxy/halo system (from A to J for ten systems), followed by a lowercase letter that is labeled “ l ” or “ h ” meaning low (218 pc) and high (109 pc) resolution, respectively, and finally by a number that is used to differentiate cases with different combinations of the parameters ϵ_{SF} and t_{off} (indicated in the next columns). There are three simulations marked with the symbol “*”. In simulations with “ h ” but without “*”, cells were refined if they satisfy the above mentioned condition *but* with m_p given by its *lower resolution* (less species) value, which is 8 times larger. Thus, the refinement condition for these simulations poorly obeys the cell scaling and the “ h ” simulations end up with a number of resolution elements close to that obtained actually for “ l ” simulations. Model galaxies with “ h ” and “*” do satisfy the scaling: cells are refined according to the above recipe with m_p given by its higher resolution value. In other words, simulations with “ h ” and “*” are of high resolu-

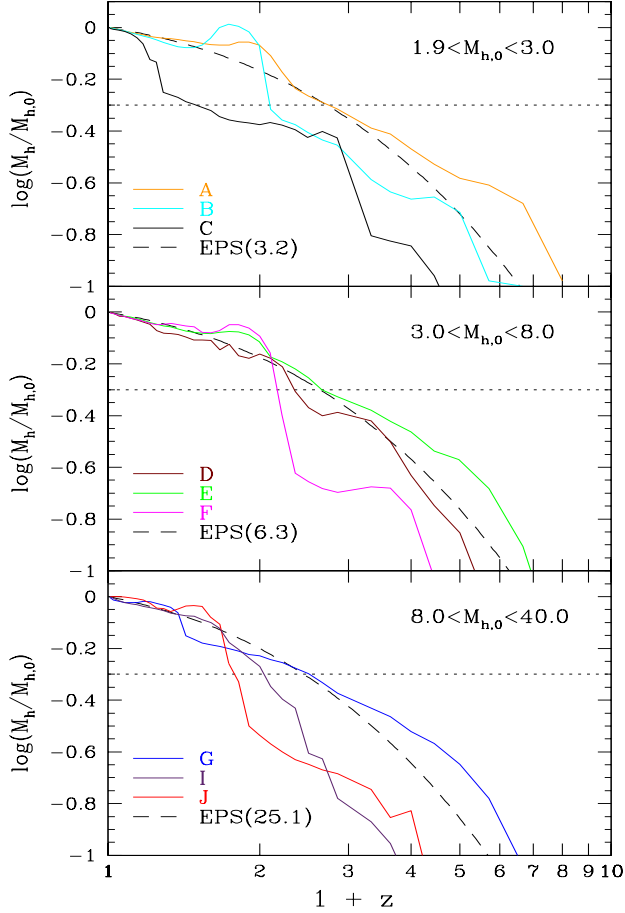


FIG. 1.— Mass aggregation histories of nine of our simulated halos normalized to the mass attained at $z = 0$, $M_{h,0}$. In each panel, the MAHs of three halos (identified with the uppercase letter) in the mass range shown in the upper-right parts of the panels are plotted ($M_{h,0}$ is in unities of $10^{10} M_{\odot}$). The dashed curves correspond to the average MAHs (20,000 realizations) of halos of $M_{h,0}$ as indicated in the parenthesis. These MAHs were calculated using the EPS formalism by Firmani & Avila-Reese (2000). The horizontal dotted lines correspond to half $M_{h,0}$.

tion in the sense of the number of DM particles and in terms of number of grid cells. As can be anticipated, the modeling of galaxies with “h” and “*” consumes a lot of CPU and wall time and thus, although desirable, not all models could be run with this resolution. In columns (2), (3), and (4) the total halo virial mass M_h at $z = 0$, the DM particle mass resolution, m_{dm} , and the size of the finest grid cell, ℓ_{max} , are reported. The values used for the parameters ϵ_{SF} and t_{off} are shown in columns (5) and (6).

Galaxies *G* and *J* are actually from one simulation, corresponding to the box used in C10. This simulation was run to get a maximum resolution of $\ell_{max} = 218$ pc (three DM particle species). Cases in which the ϵ_{SF} column is written “—” refer to the simulations where ϵ_{SF} was not fixed but was calculated at each cell and timestep by an algorithm introducing other parameters (see §§2.1 and C10). The system *E* is the one that covers the largest variation of cases and parameters.

Galaxy *H* was simulated with the stochastic approach for SF, ϵ_{SF} not fixed a priori, and without turning off the cooling. In this simulation, following Ceverino & Klypin (2009), “runaway stars” are modeled. These are massive stars with high peculiar velocities as a result of the SN explosion in a close binary or due to two-body encounters in stellar clus-

ter. As a result, runaway stars can move far away from the SF regions, being then able to inject energy into the ISM in regions of low-density gas, where the cooling time is large so the feedback efficiency is higher. The runaway stars are modeled through the addition of a random velocity, drawn from an exponential distribution with a characteristic scale of 17 km s^{-1} , to the inherited gas velocity in 30% of the stellar particles.

2.3. Halo mass aggregation histories

The halo mass aggregation histories (MAHs) of the simulations presented in Table 1, except for run *H*, are plotted in Fig. 1. The SF histories of galaxies are expected to follow in a first approximation the halo MAHs. As seen, the MAHs of the different simulated distinct halos are quite diverse, and several of them oscillate around the average Λ CDM halo MAHs expected for these masses (dashed curves calculated with the Extended Press-Schechter -EPS- formalism of Firmani & Avila-Reese 2000, which gives results in good agreement with the fits to the outcomes of the Millenium and Millenium II simulations (Fakhouri, Ma & Boylan-Kolchin 2010)⁶. Most of our simulated halos show late (since $z \sim 0.6$) MAHs close to the corresponding averages.

Halos *B*, *F*, and *J* suffer a late major merger at $z \approx 1.0$, 1.1, and 0.7, respectively. Actually, halo *F* suffers two major mergers that occur around $z = 1$; this explains the big jump in mass seen in the MAH of this halo. Halos *A* and *E* have MAHs that imply very early mass assembly. Halos *C*, *F*, *I* and *J* have MAHs implying mass assemblies later than the corresponding averages. In particular, is remarkable the delayed MAH of halo *C*. The increase in mass seen at $z \approx 0.33$ in this halo is due to the almost simultaneous accretion of three medium-sized halos each of mass of about one tenth of the mass of halo *C*, two of them coming in a pair.

It is important to remark that all the simulated halos are distinct at $z = 0$, and the galaxies studied here are the *central ones* inside these halos.

3. RESULTS AND COMPARISON WITH OBSERVATIONS

Most of the simulated galaxies studied here show dynamical, structural, and ISM properties in reasonable agreement with observations of sub- M^* central galaxies. The code SF/feedback schemes and their parameters (see §2.1) were extensively explored in C10. Based on the analysis results from that work, here we limit our experiments to only a few variations of some of the parameters and to simulations with higher resolutions (see Table 1). Our goal is to explore the SFR, M_s and M_h evolution of low-mass isolated galaxies in the numerical simulations and to compare them to current observational inferences of central sub- M^* galaxies at different redshifts.

3.1. General properties

The main properties at $z = 0$ of all runs are reported in Table 2. The simulation name and halo virial mass M_h are given in columns (1) and (2). Columns (3) and (4) present the galaxy stellar (disk + spheroid) mass and the (cold) galaxy gas mass fraction, M_s and $f_g = M_g/(M_s + M_g)$, respectively, where M_g is the mass contained in gas particles with $T \leq 10^4$

⁶ While the EPS average MAHs are for pure DM halos, the MAHs from the simulations are for the DM+baryons systems. The inclusion of baryonic physics actually does not affect significantly the halo MAHs.

TABLE 2
PHYSICAL PROPERTIES AT $z = 0$ OF SIMULATED GALAXIES

Name	M_h	M_s	f_g	R_e	V_{\max}	SFR	F_s	F_b
(1)	(2)	(3)	(4)	(5)	(6)	(7)	(8)	(9)
	($10^{10} M_\odot$)	($10^9 M_\odot$)		(kpc/h)	(km s^{-1})	($M_\odot \text{ yr}^{-1}$)		
A_{h1}	1.97	0.17	0.051	0.45	50.8	0.000	0.009	0.009
A_{h1}^*	2.01	0.30	0.058	0.31	52.9	0.000	0.015	0.016
B_{h1}	2.32	0.22	0.440	0.59	49.4	0.003	0.009	0.017
B_{h1}^*	2.46	0.21	0.690	0.50	55.9	0.009	0.009	0.027
C_{l1}	2.80	0.10	0.850	0.66	57.1	0.000	0.004	0.023
C_{h1}	2.48	0.21	0.480	0.94	44.2	0.006	0.009	0.016
C_{h1}^*	2.84	0.16	0.760	0.74	51.4	0.012	0.006	0.024
D_{h1}	3.65	0.44	0.620	0.66	60.9	0.013	0.012	0.032
E_{l1}	5.94	3.47	0.100	0.55	126.0	0.110	0.058	0.065
E_{h1}	5.11	1.84	0.048	0.83	82.2	0.016	0.036	0.038
E_{h2}	5.31	2.02	0.340	1.05	84.0	0.044	0.038	0.058
E_{h3}	5.76	3.56	0.280	0.80	104.8	0.062	0.062	0.086
F_{l1}	7.79	5.01	0.350	0.84	124.1	0.360	0.064	0.099
F_{h1}	6.56	3.74	0.072	0.97	87.5	0.038	0.057	0.061
G_{l1}	8.37	3.88	0.110	0.67	125.9	0.120	0.046	0.052
G_{l2}	9.52	7.82	0.220	0.55	185.0	0.650	0.082	0.106
H_{l1}	14.5	10.0	0.054	1.03	188.0	0.120	0.069	0.073
I_{l1}	30.4	22.8	0.170	1.10	254.8	0.480	0.075	0.090
I_{h1}	30.5	25.4	0.230	1.75	213.3	0.150	0.083	0.108
J_{l1}	35.8	20.9	0.070	1.21	214.3	0.150	0.058	0.063
J_{l2}	40.4	29.2	0.140	0.85	279.2	0.370	0.072	0.084

K. Both M_s and M_g are defined as the stellar and gas mass contained within $5R_e$, where R_e is in turn defined as the radius where half of the galaxy stellar mass is contained (column 5). This latter mass is found inside the radius defined as the minimum between the tidal and 0.5 the halo virial radius. This definition considers the stellar mass associated with a possible very extended stellar halo; satellite galaxies would be also considered, but this makes no difference as far as R_e and related properties are concerned because their contribution to the total mass is $\lesssim 5\%$. The maximum circular velocity, V_{\max} , is given in column (6); the circular velocity is computed as $V_c = \sqrt{GM(R)/R}$, where $M(R)$ is the total (dark, stellar, and gas) mass. Finally, columns (7) and (8) give the galaxy stellar and baryon mass fractions, defined as $F_s = M_s/M_h$ and $F_b = M_b/M_h$, where $M_b = M_s + M_g$ and M_h is the total (dark+baryon) virial mass.

In Figure 2, V_{\max} vs M_s (the stellar Tully-Fisher relation, sTFR, panel a) and R_e vs M_s (panel b) at $z = 0$ are plotted for all simulated galaxies (geometric symbols). The black solid and dotted lines show linear fits and their estimated 1σ intrinsic scatters to observed normal disk galaxies in a large mass and surface density range as reported in Avila-Reese et al. (2008). Their stellar masses were corrected by -0.1 dex to go from the ‘diet Salpeter’ IMF (Bell et al. 2003) implicit in their inferences to the Chabrier (2003) IMF.

Big and small geometric symbols are used for high- and low-resolution runs, respectively. The symbols are open when $t_{\text{off}} = 40$ Myr and solid when $t_{\text{off}} = 20$ or 10 Myr. Circle, pentagon, and square are used for runs where $\epsilon_{\text{SF}} = 0.5$, 0.2, and 0.67, respectively; a triangle is used when the stellar mass particle is calculated rather than assigned as a fraction of the gas mass cell (see §2.2). The runs that correspond to the same galaxy/halo system have the same color. Symbols traversed by a cross correspond to high-resolution simulations with more grid cells (A_{h1}^* , B_{h1}^* , and C_{h1}^*). The open inverted triangle corresponds to the simulation with the run-away stars

scheme and without turning off cooling.

From upper panel of Fig. 2, one clearly sees that the low-resolution simulations produce galaxies with too large values of V_{\max} for their masses. It is well known that the lack of resolution in this kind of simulations introduces an artificial dissipation of energy and angular momentum in the gas, producing these too-concentrated galaxies and therefore, peaked rotation curves (as well as less SF and energy input to the gas, in such a way that galaxy outflows are inefficient, having then the galaxies too high baryonic and stellar fractions, see Table 2). However, our high-resolution simulations are already in rough agreement with the observationally-inferred sTFR, except for the run *I*. In general, the mid-plane gas disk rotation velocity profile, $V_{\text{rot}}(R)$, is lower than $V_c(R)$ in the inner regions (e.g., Valenzuela et al. 2007, C10), and in some cases, even the maximum of $V_{\text{rot}}(R)$ may be slightly lower than V_{\max} . Therefore, when comparing with observations, V_{\max} tends to be an upper limit. In Fig. 2 we also reproduce results from other recent high-resolution simulations (Governato et al. 2007, 2010; Piontek & Steinmetz 2011), where the problem of obtaining a TFR shifted to the high-velocity side seems to have been partially overcome (see §§4.1 for details on these works).

Our smallest simulated galaxies fall systematically above the extrapolated sTFR of higher masses, suggesting a bend towards the low M_s (high V_{\max}) side. Such a bend at low masses in the sTFR has been discussed recently by de Rossi et al. (2010), who explain it as a consequence of the strong stellar feedback-driven outflows. From the observational side, some authors have found that the infrared or stellar TFRs at low masses become very scattered but apparently M_s is on average lower for a given V_{\max} than the extrapolation of the high-mass sTFR (e.g., McGaugh 2005; Geha et al. 2006; De Rijcke et al. 2007). In the upper panel of Fig. 2, the observational data for dwarf galaxies reported in Geha et al. (2006) are reproduced (dots).

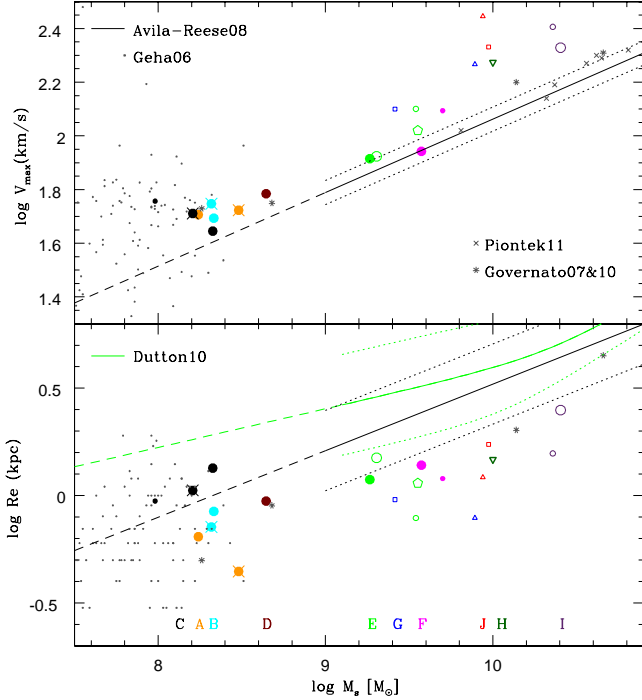


FIG. 2.— Maximum circular velocity (upper panel) and effective radius (lower panel) vs. M_* for the different galaxies simulated here (figure symbols, see text for the symbol code and Table 1 for the color/letter code showed below in lower panel). The small skeletal symbols are for the simulations from Piontek & Steinmetz (2011) and Governato et al. (2007, 2010). The fits and 1σ intrinsic scatters in both panels to a compiled sample of normal disk galaxies by Avila-Reese et al. (2008) are plotted with solid and dotted lines, respectively. The observed dwarf galaxies by Geha et al. (2006) are also plotted (dots). In lower panel, the fit to the blue-cloud disk-dominated galaxies from the SDSS by Dutton et al. (2010b) is reproduced (green solid line; the dotted lines show the 84th and 16th percentiles of the size distribution). The dashed lines are extrapolations to lower masses of the given fits.

Regarding the R_e – M_* relation, the lower panel of Fig. 2 shows that the low-resolution simulations produce too concentrated galaxies, in agreement with the resolution arguments already mentioned above. However, even for the high-resolution simulations, our most massive modeled galaxies have radii smaller than the mean of the observational inferences for a given M_* . In Fig. 2 is also plotted the fit to the R_e – M_* relation inferred recently by Dutton et al. (2010b) for the blue-cloud disk-dominated galaxies from the SDSS (green solid line). These inferences show a pronounced bend (flattening) in the R_e – M_* relation at low masses ($M_* \lesssim 2 \times 10^{10} M_\odot$). The measured radii for dwarf galaxies from Geha et al. (2006) are also reproduced in Fig. 2 (dots). These galaxies lie clearly below the extrapolation of the the Dutton et al. (2010b) R_e – M_* relation, but agree with the extrapolation of the Avila-Reese et al. (2008) relation. Our lowest-mass simulations show better agreement with observations.

It should be noted that R_e both in Avila-Reese et al. (2008) and Dutton et al. (2010b) was calculated assuming $R_e = 1.67R_d$, where R_d is the scale radius obtained from fitting an exponential law to the disk component of the surface brightness profile. The above relation is a good approximation if most of the stellar mass lies in a disk; however, if the bulge/spheroidal component is non-negligible, then the actual effective radius R_e is expected to be different from $1.67R_d$. For several of our high-resolution simulations, we have found that R_e is smaller than $1.67R_d$ by factors of $\sim 1.1 - 1.3$, not enough to explain the differences seen in Fig. 2 for the more

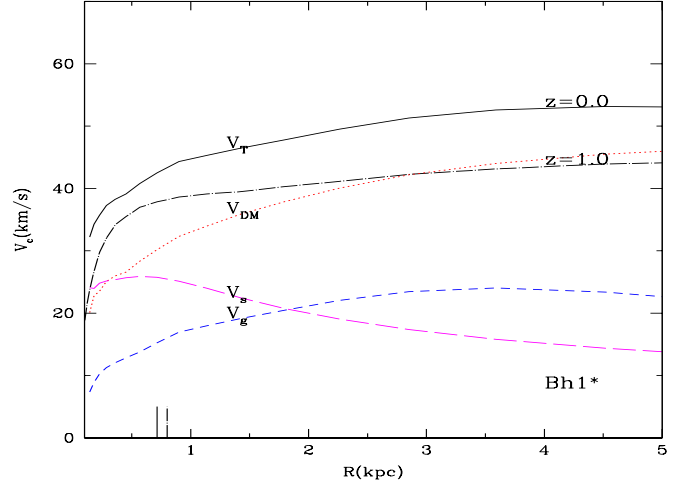


FIG. 3.— Circular velocity profile, $V_c(R)$, at $z = 1$ (thick dot-dashed line) and $z = 0$ (solid line) of run B_{h1}^* . The velocity components at $z = 0$ corresponding to dark matter (dotted red line), galaxy stars (long-dashed pink line), and galaxy gas (short-dashed blue line) are also plotted. The vertical segments above the x-axis indicate $1R_e$ at $z = 1$ and $z = 0$.

massive galaxies. In some cases, R_e results even larger than $1.67R_d$.

The structure of the stellar component of normal low-mass and dwarf galaxies seems to be different from the usual one of normal high-mass galaxies, both from the point of view of observations and simulations. In particular, the existence of an extended spheroidal component could be the rule as seen in our lowest-mass simulations (see also C10; Bekki 2008, and therein references on observational works). In general, the stellar surface density profiles of our simulated galaxies tend to be exponential within $\sim 1 - 3 R_e$.

Regarding the circular velocity profiles, $V_c(R)$, they are roughly flat at $1.5 - 3 R_e$ for all the high-resolution runs except for the most massive one, I_{h1} , which shows a narrow peak at $0.2R_e$. In some cases, $V_c(R)$ is even slightly increasing at $1 - 2 R_e$ as it is the case of run B_{h1}^* , shown at $z = 0.0$ (solid line) and 1.0 (thick dot-dashed line) in Figure 3. For our lower-resolution simulations, in some cases the velocity profiles are peaked. As expected, $V_c(R)$ increases with time. The decomposition of $V_c(R)$ into the dark matter (DM), stellar (s) and gas (g) components is also plotted in Fig. 3, for the $z = 0$ profile. This galaxy is dark-matter-dominated for radii $\gtrsim 1R_e$. The effect of stellar feedback is crucial in order to prevent excessive baryon matter concentration in the center –and consequently a peaked $V_c(R)$ profile– as has been discussed in C10 (see also Governato et al. 2007; Ceverino & Klypin 2009; Stinson et al. 2009).

Figure 4 presents the “archeological” SF histories (SFHs) for our high-resolution runs, defined as the instantaneous SFR as a function of time, and computed for each run using the last snapshot recorded. Specifically, in each data dump, in addition to the positions and velocities for all stellar particles, the code also saves the time at which they formed, their masses (initial and present), and metallicities due to SNe of types Ia and II. We add up the (initial) masses of the stellar particles formed during a certain time interval, which we take as 0.5 Gyr, and divide it by this time, to obtain the “instantaneous” SFR. Since the amount of stellar mass outside the galaxy is typically a small fraction, the SFH computed inside R_{vir} is mostly that of the central galaxy. Unlike C10, where a time interval of 0.1 Gyr was taken to compute the SFHs, here we use

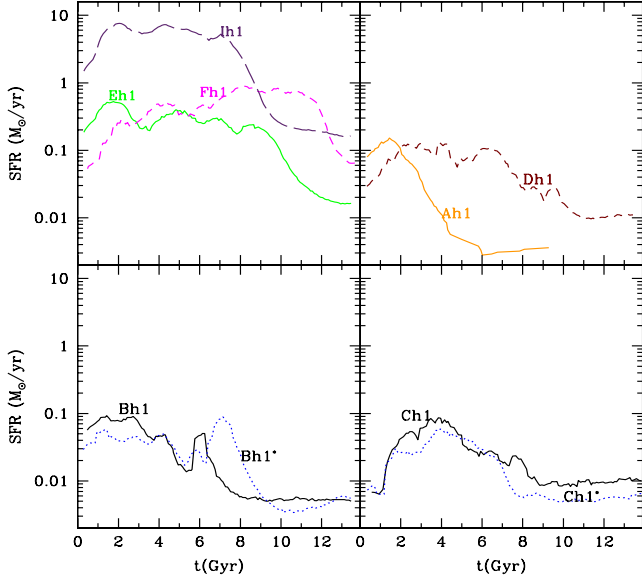


FIG. 4.— “Archaeological” SFHs from the high-resolution runs. Top-panels: I_{h1} , F_{h1} , E_{h1} runs (left panel) and D_{h1} , A_{h1} runs (right panel). Lower-panels: A comparison of the B run with and without “*”; that is, run with a low and high number of cells inside R_{vir} (left panel). Right-panel: Same as in left panel but for run C . With the exception of run F_{h1} , models show a much smaller SFR in the last 5-6 or more Gyr with respect to the previous, active, early epoch.

0.5 Gyr in order to produce smoother SFHs. To estimate how much the SFR fluctuates, for example, in the last 1 Gyr, we measured the SFR in bins of 0.1 Gyr width and computed the dispersion of data for each run. We find dispersions around the means of about 30-40%.

In the top panels, the “archaeological” SFHs of runs I_{h1} , F_{h1} , E_{h1} (left panel), and D_{h1} , A_{h1} (right panel), are plotted, using the same color coding as in Figure 1. In the lower-left panel, we compare the SFHs of run B simulated with a high number of DM matter particles but with a low (dotted blue lines) and high (solid black lines) number of cells. The same comparison but for run C is shown in the lower-right panel. As can be seen, there is not a significant difference in their SFHs between models with “*” and those without it. The SFHs are diverse but in most cases they are characterized by an active phase that starts after the first 1-2 Gyr and lasts 2-6 Gyr. This phase is followed by a “quiescent” stage with a low value of the SFR, with most of the SF concentrated in the central part of galaxies. In most cases, the SFHs inherit some features of the halo MAHs. The “archaeological” SFHs already forecast that simulated low-mass galaxies will have low SSFRs at late epochs in conflict with observational inferences.

Finally, it should be said that in almost all of our simulations a multi-phase ISM develops in the disks (see for more details C10). This results from the efficiency by which thermal energy is injected into the ISM and the ability of the medium to self-regulate its SF.

3.2. Specific star formation rate as a function of mass

The main result of this paper is shown in Figure 5, where the *directly* measured galaxy SSFR of the simulations at four epochs ($z = 0.00, 0.33, 1.00$ and 1.50) are plotted vs the corresponding current stellar masses (geometric symbols). For the symbol code and color/letter code, see previous subsection. Unlike the “archaeological” SFR shown in Fig. 4, here

the SFR at a given redshift is computed by summing up the mass of all stellar particles with ages smaller than 0.1 Gyr located in a cylinder with $1.0 h^{-1}\text{kpc}$ (proper) height and $20.0 h^{-1}\text{kpc}$ of radius, centered on the gaseous disk. The SFR is then this mass divided by 0.1 Gyr. This time bin is wide enough so as to avoid short fluctuations in the SFR values.

The general trend of the measured SSFR in the simulations is to decrease with time, though, in general the SFR (and therefore SSFR) histories are quite episodic (see also Fig. 4). It is remarkable that at low redshifts ($z = 0$ and 0.33), all simulated galaxies have SSFRs below the SSFR a galaxy would have if it had formed all stars at a constant SFR⁷ (horizontal dashed line). This means that the M_s of these galaxies was assembled relatively early, the current SFRs being smaller than their past average SFRs (the galaxies entered into a quiescent SF phase). For higher redshifts, $z = 1.00$ and 1.50 , the SSFRs of several of the *high-resolution* simulations tend to be already around the $\text{SFR}=\text{const.}$ line, which means that galaxies are in their active phase of SF and M_s assembly.

Notice that some runs show negligible SSFRs at some epochs. For example, the SSFR of run A_{h1}^* is zero at $z = 0.0$ (the halo MAH of this run is the earliest one among all simulations, see Fig. 1, which seems to imply that its SFR decreased strongly very early, see Fig. 4). Because of the episodic nature of the SFR it may well be that, even though we use a relatively wide time bin to compute the instantaneous SFR (0.1 Gyr), there are some epochs for which we see a galaxy almost not forming stars. Run C_{l1} is special in the sense that it has zero SFR at the time-steps corresponding to $z = 0$ and $z = 0.33$, something that is not seen for the higher-resolution counterpart simulations. The resolution in this case seems to affect the efficiency of SF because the galaxy actually is growing plenty of gas ($f_g = 0.85$ and 0.70 at $z = 0$ and 0.33 , respectively; note that the halo MAH of this model shows the most active growth at late epochs). This is probably because instabilities in the disk have not been resolved. Indeed, in the corresponding high-resolution runs, specially the C_{h1}^* one, a relative high SSFR is measured at late epochs. However, there are cases of high-resolution simulations, for example run D_{h1} , where the gas fraction is high and even increases at late epochs, but the SSFR keeps low and decreasing with time. We suspect that in these cases some physical process is damping the disk gas instabilities, and therefore inhibiting active SF; the presence of a dynamically hot spheroid—which is actually formed in several of our low-mass simulations—has been shown to work in this direction (Martig et al. 2009).

From Fig. 5 one sees that the resolution affects moderately the SSFRs. Our low-resolution simulations tend to have lower values of SSFR at $z = 1.50$ and 1.00 than the high-resolution ones, but the opposite applies for lower z . At this point, it should be said that it is difficult to establish any systematicity due to the episodic behavior of the SFR in the simulations. At $z = 0$, low-resolution simulations seem to produce slightly higher SSFR values than high-resolution simulations. Note also that the former have systematically higher values of f_g than the latter (see Table 2). The effect of increasing the number of cells (filled circles traversed by a cross) is not so significant. The global effect of the strength of the stellar feedback (regulated in our simulations by ϵ_{SF} and t_{off}) apparently is to

⁷ If $\text{SFR}=\text{const.}$ in time, then $\text{SFR}/M_s = 1/[(1-R)(t_H(z) - 1 \text{ Gyr})]$, where $R = 0.4$ is the average gas return factor due to stellar mass loss, t_H is the cosmic time, and 1 Gyr is subtracted in order to take into account the onset of galaxy formation.

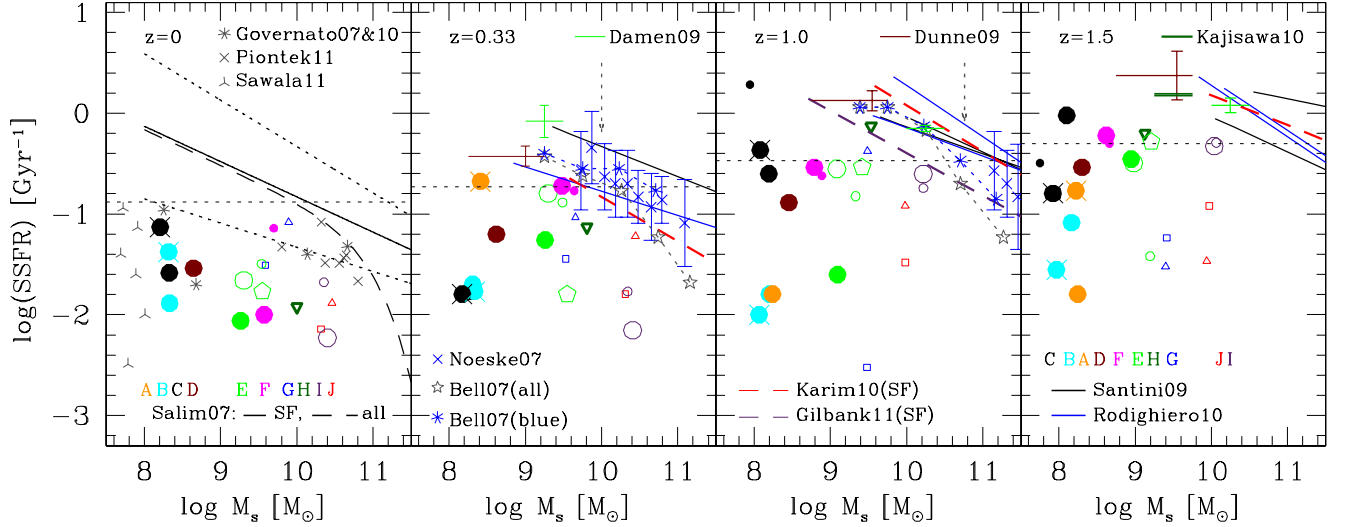


FIG. 5.— SSFR vs M_s measured at four different redshifts for all of our simulations (geometrical symbols). A given galaxy is represented with the same color (associated to the letter that identifies the simulation according to Table 1), and the different symbols are to distinguish runs of the same galaxy but with different sub-grid parameters (see §§. for the symbol code). The horizontal dotted lines in each panel correspond to the SSFR of a galaxy that had a constant SFR in the past (see text); galaxies above (below) this line are expected to have been less (more) active in forming stars on average in the past than in the current epoch. In the $z = 0$ panel results from simulations by Governato et al. (2007, 2010), Piontek & Steinmetz (2011), and Sawala et al. (2011) are also plotted; the solid line is the linear fit carried out by Salim et al. (2007) to the sub-sample of star-forming galaxies from a volume-corrected sample of $\sim 50,000$ SDSS galaxies (the intrinsic scatter is shown with dotted lines), while the long-dashed line is the Schechter fit to the entire sample, i.e. including composite galaxies (SF/AGN), galaxies dominated by AGN emission, and those with no $H\alpha$ detection. The skeletal symbols, fit lines, and horizontal segments in the high-redshift panels correspond to different observational estimates down to the completeness limits reported in the works indicated inside the panels (see Appendix for a description of each one of them). At all the epochs reported here, the observationally estimated SSFRs of low mass-galaxies are on average significantly higher than those of simulations. While observational estimates at each one of the redshifts are typically above the SFR=const. lines for low masses, the simulations are in most cases below them, specially for $z < 1$.

keep the SF more active at later epochs as seen for runs E_{h1} ($t_{\text{off}} = 10$ Myr, open green circle) and E_{h2} ($t_{\text{off}} = 40$ Myr, filled green circle). However, the differences are small, as in the case of variations in ϵ_{SF} from 0.5 to 0.2 (runs E_{h2} , filled green circle, and E_{h3} , filled green pentagon, respectively). In general, variations of the sub-grid parameters around reasonable values seem not to be a source of significant and systematic changes in the SSFR of the simulated galaxies.

3.2.1. Comparison with observational inferences

In each panel of Fig. 5, different observational inferences compiled here are plotted for comparison. Unless otherwise stated, we plot only the data that obey the completeness limit given by the different authors. The inferences of M_s (and SFR) from the observed luminosities or spectral energy distribution of galaxies are based on results from SPS (stellar population synthesis) models. For all cases reproduced in Fig. 5, a constant, universal, stellar initial mass function (IMF) has been assumed in these models, although different authors may have used different IMFs. We homogenize all observational results to a Chabrier (2003) IMF (see Appendix for the different corrections applied here). A description of each one of the observational sources compiled from the literature is presented in the Appendix.

From a visual inspection of Fig. 5 we conclude that all simulated low-mass galaxies at different resolutions and sub-grid parameters lie significantly below the averages of a large body of SSFRs observational determinations as a function of M_s out to $z \sim 1.5$, especially for the blue star-forming ones. In the $z = 0$ panel, a compilation of recent numerical results from other authors are also plotted (skeletal symbols; see §4.1 for more details).

By taking into account only our high-resolution simulations with $\epsilon_{\text{SF}} = 0.5$, we estimate that the SSFRs in the mass range

$M_s \sim 10^8 - 10^{10} M_\odot$ are $\sim 5 - 10$ times lower than the means inferred from observations at $z \approx 0$. These differences are roughly the same or slightly smaller at $z \approx 0.33$. At higher redshifts ($z \approx 1.0 - 1.5$), the comparison becomes difficult by the incompleteness in the observational samples. However, both for the small mass range where our simulations coincide with observations above the completeness limit and the extrapolations to lower masses of the inferred SSFR- M_s relations, the differences persist, though they are less dramatic than at lower z .

It is notable the systematical shift of the SSFR- M_s relation of observed galaxies as z decreases: from a rough average of all relations, the typical stellar mass, M_{quench} , that crosses below the line corresponding to the constant SFR case at each z (horizontal short-dashed lines in Fig. 5) decreases with time. In other words, the lower the z , the smaller on average are the galaxies that start quenching their SF (downsizing in SSFR). Interesting enough, the downsizing of M_{quench} is in rough quantitative agreement with the downsizing of the transition mass from active to passive galaxies found from the semi-empirical M_s growth tracks in FA10: $\log M_{\text{tran}}(z) = 10.30 + 0.55z$. For the simulated galaxies, there is no evidence of such a phenomenon of downsizing.

3.3. Stellar mass fraction as a function of mass

In Fig. 6 the stellar mass fraction, $F_s \equiv M_s/M_h$, of our simulated galaxies vs M_h at $z = 0.00, 0.33, 1.00$ and 1.50 are plotted. Results from numerical simulations of other authors shown in Fig. 5 are also plotted (skeletal symbols).

The bell-shaped curve in each panel corresponds to the continuous analytical approximations given in FA10 to the semi-empirical determinations of the M_s - M_h relations at different redshifts ($0 \lesssim z < 4$) performed by Behroozi et al. (2010). These inferences are based on the abundance match-

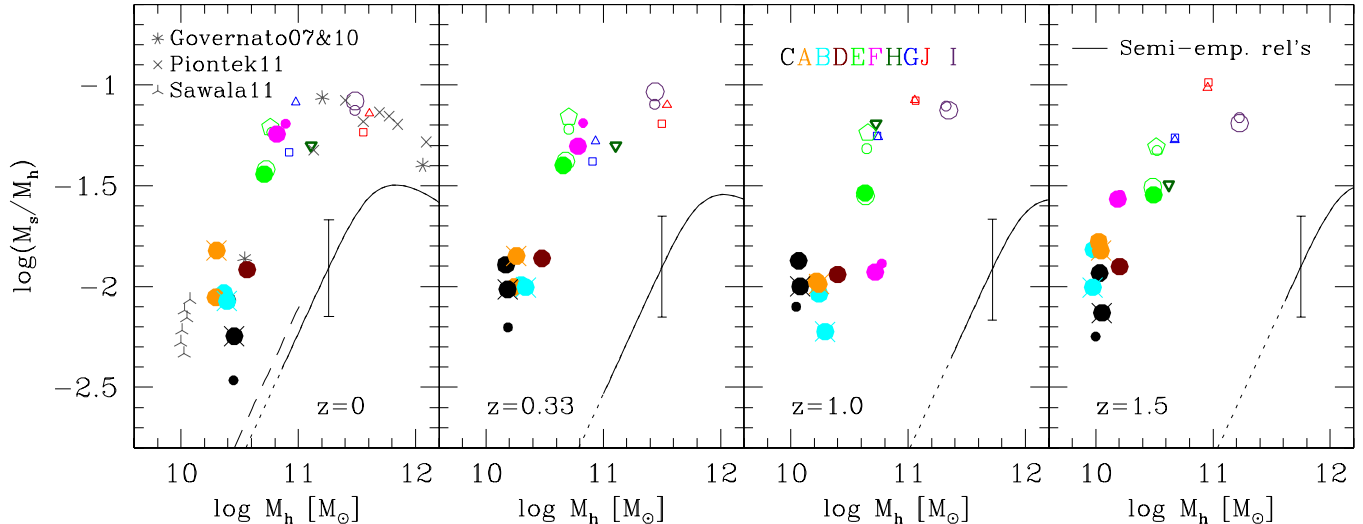


FIG. 6.— Stellar mass fraction vs M_h of the simulated galaxies at $z = 0, 0.33, 1$, and 1.5 (geometrical symbols). The symbol and color/letter codes are as in Fig. 5. The results from other authors (indicated inside the panel) are also reproduced for $z = 0$. The solid curves in each panel are semi-empirical inferences as reported in FA10 based on Behroozi et al. (2010). The error bars show the 1σ uncertainty of these inferences. The dotted lines are extrapolations to lower masses, given the lower limits in M_s of the empirical galaxy M_s functions used in Behroozi et al. For the dashed line in the $z = 0$ panel see the text.

ing formalism, where the cumulative observed galaxy stellar mass function at a given epoch is matched to the cumulative halo mass function in order to find the M_h corresponding to a given M_s , under the assumption of a one to one galaxy-halo correspondence. Several authors have found similar results out to $z \sim 1$, even when different observational data sets and formalisms have been used (see for recent results e.g., Moster et al. 2010; Guo et al. 2010; Wang & Jing 2010). For the local universe, direct techniques, as galaxy-galaxy weak lensing and satellite kinematics, have also been applied to infer the M_s – M_h relation with results that are in reasonable agreement among them and with other techniques (see for comparisons Behroozi et al. 2010; More et al. 2010; Rodríguez-Puebla et al. 2011, and more references therein) in the mass ranges where they can be compared (the direct techniques are reliable for the time being only for intermediate or massive galaxies). The error bar in Fig. 6 indicates the approximate $\pm 1\sigma$ statistical and sample variance uncertainties in the inferences. The main contributor to this uncertainty comes from assumptions in converting galaxy luminosity into M_s (Behroozi et al. 2010).

According to Fig. 6, the smaller is the mass, the lower is F_s on average, both for our simulations and the semi-empirical inferences. However, the simulation results have F_s values systematically higher than those inferred from observations. At $z \approx 0$, the differences amount to factors around 5–10 and they apparently increase at higher redshifts; at $z = 1.5$, the simulations have values of F_s for a given M_s around 30 times higher than those inferred semi-empirically at the masses where the comparison can be done; the same factor applies for the lowest masses if one extrapolates the semi-empirical determination to these masses. For simulated galaxies, F_s changes very little in the redshift range reported here while halo masses decrease as z increases. Therefore one expects the F_s – M_h relation to shift on average to the low-mass side as z gets higher. This behavior is contrary to the semi-empirical inferences.

In the semi-empirical inferences, the mass function of pure dark matter halos is used. It could be that the masses of the halos (dark+baryonic matter) end up smaller when baryonic processes are included; for example, as a result of mass loss

out the virial radius in low-mass halos. The maximum fraction of ejected baryons at $z = 0$ in our simulations is 82% for runs A_{h1}^* and B_{h1}^* ⁸. This would imply that M_h in run A_{h1}^* (or B_{h1}^*) is $\approx (1 - 0.82F_{b,U})^{-1} = 1.14$ times smaller than in a purely dark matter simulation. The dashed line in Fig. 6, $z = 0$ panel, shows the expected shift in the M_s/M_h – M_h relation by this maximum factor. On the other hand, the inferred M_s/M_h ratio at low masses depends mainly on what is the faint-end slope of the galaxy M_s function. If observations show that there is a steepening of this slope, then the M_s/M_h ratio may flatten at low masses, being in better agreement with our simulation results. Some recent observational studies suggest that the higher the z (for $z \gtrsim 1$), the steeper is the faint-end slope (Kajisawa et al. 2009; Mortlock et al. 2011). For lower z , there is also evidence of a somewhat steep slope (~ -1.7 , e.g. Drory et al. 2009). However, even that, the M_s/M_h – M_h relation at low-masses seems to be steeper and lower than in our simulations (see Fig. 9 in Drory et al. 2009).

In Fig. 7, we have merged into one the four panels (epochs) of Fig. 6, showing the evolution (connected with dotted lines) of only some of our high-resolution simulations. The relatively large jumps seen in some runs are mainly due to halo major mergers. For example, run F_{h1} shows a strong decreasing of $F_s = M_s/M_h$ at $z \approx 1$ because it suffered major mergers around this epoch (see Fig. 1). For simulations where the halo MAH tends to be smooth, F_s changes more smoothly with z (e.g., runs D_{h1} , E_{h1} and I_{h1}).

We also plot in Fig. 7 the evolution of two semi-numerical models presented in FA10. These models correspond to the case of energy-driven SN outflows and no re-accretion, with an outflow efficiency of 65%; only with such a high efficiency it is possible to lower the stellar mass fractions to roughly agree with the F_s – M_h determinations at $z = 0$.

For both cases, simulations and semi-numerical models, F_s changes relatively little with z . As mentioned in the Introduction, FA10 (see also Conroy & Wechsler 2009) connected the F_s – M_h relations by using *average* MAHs and obtained the

⁸ For other mass runs with $M_h < 3 \times 10^9 M_\odot$, this fraction vary around 60–80%, while for the more massive runs the fractions are 10 – 40%.

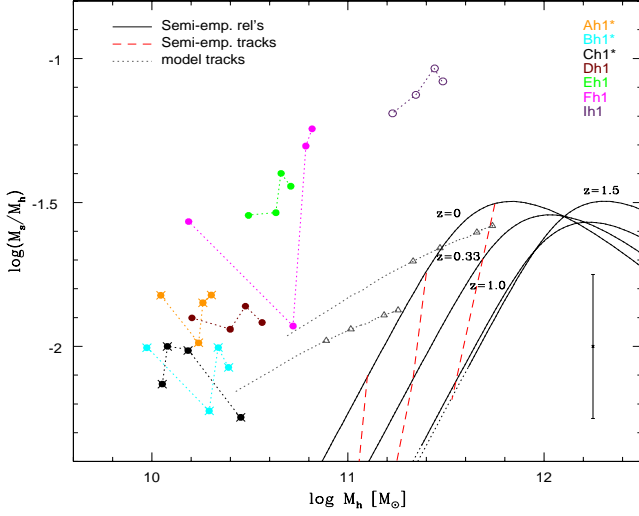


FIG. 7.— Stellar mass fraction vs M_h at $z = 0, 0.33, 1.0$ and 1.5 for the high-resolution runs indicated inside the panel, and for two semi-numerical models presented in FA10 (open black triangles; the dotted lines extend up to $z = 4$). The solid black curves are the same semi-empirical determinations plotted in Fig. 6 at the four epochs mentioned above. The dashed red curves correspond to three semi-empirical individual *average* evolutionary tracks (GHETs) as inferred in FA10.

corresponding *individual* (average) F_s (or M_s) hybrid evolutionary tracks (GHETs, dashed red curves in Fig. 7). These tracks in the $\log M_s(z)$ (or $\log F_s$)- $\log M_h(z)$ plane have very steep slopes for low-mass galaxies, $d\log M_s(z)/d\log M_h(z) \sim 4.5$ ($z < 1$), i.e. for these galaxies, M_s (F_s) grows very fast since $z \sim 1$. However, for the semi-numerically modeled galaxies, $d\log M_s(z)/d\log M_h(z) \sim 1.4$, i.e. M_s (F_s) grows slowly. *Our numerical simulations, albeit noisily, confirm such a behaviour, which strongly disagrees with the semi-empirical tracks.*

4. DISCUSSION

We would like to stress that (i) the potential issues of low-mass Λ CDM-based simulated galaxies showed in Figs. 5 and 6 seem to be shared by most previous high-resolution numerical simulation works, and (ii) that the empirical inferences we have compiled in this paper are yet subject to large uncertainties and probable systematical errors. Following, we discuss both items.

4.1. Previous numerical works and numerical issues

In Figs. 2, 5 and 6 we have reproduced the $z = 0$ properties of sub- M^* galaxies presented in recent numerical works, where very high-resolution re-simulations of individual low-mass galaxies were carried out and the quantities we are interested in were reported.

The simulations by Governato et al. (2007, 2010) (asterisks in Figs. 2, 5, and 6) were performed with GASOLINE, a N-body + Smoothed Particle Hydrodynamics (SPH) code. The SF prescription ensures that the SFR density is a function of the gas density according to the observed slope of the Kennicutt-Schmidt law, and a SF efficiency parameter sets the normalization of this relation. In order to allow for SN-driven expanding hot bubbles in the non-resolved regions, cooling is turned off in the gas particles receiving SN energy until the end of the snowplow phase according to the Sedov-Taylor solution. For the force resolutions of $\sim 100 - 200$ pc achieved in their low-mass simulations, Governato et al. (2010) used a

high value for the SF density threshold, $n_{\text{SF}} = 100 \text{ cm}^{-3}$ (for the high-mass simulations in Governato et al. 2007, $n_{\text{SF}} = 0.1 \text{ cm}^{-3}$ was used), in order to have enhanced gas outflows that remove low angular momentum gas from the central regions of the galaxy; according to the authors, this helps to create realistic disks.

The simulations by Piontek & Steinmetz (2011) (crosses in Figs. 2, 5, and 6) were performed with GADGET-2, a Tree-PM N-body + SPH code. The SFR was implemented according to a Schmidt law, $\dot{\rho}_* = c_* \rho_g / t_{\text{SF}}$, where c_* is a SF efficiency parameter, and a stochastic approach for assigning stellar particles to the gas particles masses was used. Cooling is turned off in the gas particles receiving SN energy by a fixed time, 20 Myr. We reproduce here their “standard model” high-resolution simulations (gravitational softening parameters of 100–140 pc). With few exceptions, they find little or no angular momentum deficiency in their galaxies, though prominent bulges persist in most cases and galaxies lie slightly shifted in the stellar TFR.

The simulations by Sawala et al. (2011) (skeletal triangles in Figs. 5 and 6) correspond to six representative low-mass halos ($M_h(z=0) \sim 10^{10} M_\odot$) extracted from the Millenium-II Simulation. These halos were resimulated at high resolution with gas (dark and stellar mass particles of 8×10^4 and $1.8 \times 10^4 M_\odot$, respectively) using the Tree-PM code GADGET-3, which includes metal-dependent cooling, SF (Schmidt law and stochastic approach), chemical enrichment, and energy injection from type II and Ia SNe implemented in a multiphase gas model developed in Scannapieco et al. (2006). SN energy is shared equally between the hot and cold phases. Cold particles which receive SN feedback accumulate energy until their thermodynamic properties raise to the typical properties of the local hot phase. The gravitational softening scale within the collapsed halo is 155 pc. The final simulated objects have structures and stellar populations consistent with observed dwarf galaxies

On one hand, as seen from Figs. 2, 5 and 6, in most cases the properties of simulated (central) low-mass galaxies for a given M_s , in particular SSFR and F_s , agree among different authors including our results, in spite of the different codes used, simulations settings, and sub-grid physics, as well as the diversity in halo MAHs. On the other hand, all these simulated galaxies tend to have realistic structural, dynamical, and gaseous properties, excepting the *too high SSFR and too low F_s values at a given M_s* as compared with observational inferences out to $z \sim 1$.

As said in the Introduction, by increasing the resolution and including adequate SF/feedback prescriptions, several of the difficulties found in previous numerical simulations of disk galaxies have been overcome, specially the one related to the angular momentum catastrophe. According to simulation results, a key physical ingredient in the evolution of disk galaxies is the SF-driven feedback (see discussions in C10 and in the above mentioned references): it self-regulates SF promoting a multi-phase ISM; it removes low angular momentum gas from the galaxy avoiding this way the formation of a too compact stellar component with very old stellar populations; it drives galaxy outflows that lower the baryonic and stellar mass fractions in the simulated galaxies. Most authors agree that without a highly efficient SF-feedback, realistic galaxies are not reproduced. In our simulations, such an efficiency is attained by artificially turning off the cooling by a time t_{off} (only) in the cells where stars form (§§2.1). The times t_{off} used here (10–40 Myr) correspond roughly to the time a

pressure-driven super-shell takes to reach $\gtrsim 100 - 150$ pc. This latter scale corresponds roughly to our spatial resolution limits. Tests show that for t_{off} varying in the 10-40 Myr range, our results do not change significantly; compare, for example, runs E_{h1} and E_{h2} .

Regarding SF, the density and efficiency parameters used in the SF schemes, showed to be dependent on the resolution of the simulation (e.g., Saitoh et al. 2008; Brooks et al. 2011) and interconnected with the feedback and gas infall processes. From physical considerations (see C10), for the spatial resolutions achieved here, the value for n_{SF} we adopted is 6 cm^{-3} . If n_{SF} is increased to $50 - 100 \text{ cm}^{-3}$ as in Governato et al. (2010), then our low-mass galaxies become too concentrated and having too early SF (see also C10).

The lack of resolution at the scales where SF and the SF-driven momentum and energy injection to the ISM happen, remains as a shortcoming of numerical simulations, in spite of the mentioned improvements in the implementation of sub-grid schemes. The sub-grid schemes are typically "optimized" to reproduce present-day galaxy properties and for following the highest density regions of the simulation, where galaxies form. Less attention has been given to the physics of the intra-halo and intergalactic medium. The processes related to this medium could play a relevant role in galaxy formation and evolution, in particular at the early epochs and for low-mass halos.

It is not clear whether the main physics and evolutionary process of disk galaxy evolution are already captured by our and other simulations and the challenge remains only in improving resolution and tuning better the combination of small effects (e.g., Piontek & Steinmetz 2011) or some key physical ingredients and evolutive processes are yet missed. The answer to this question is beyond the scope of this paper. However, the results and discussion presented here point out to a potential serious shortcoming of simulations and models of low-mass central galaxies in the context of the Λ CDM scenario. The solution to such a problem requires that the stellar mass assembly of galaxies in distinct low-mass halos be significantly delayed to late epochs, and the smaller the galaxy, the more should be such a delay (downsizing).

4.2. Observational caveats

In the last years we have seen an explosion of works aimed to determine the stellar mass and SFR of galaxies at different redshifts (see Introduction and Appendix for references). Yet these inferences should be taken with caution, though the problem stated in this paper seems to be robust. Following, we discuss the main concerns about these inferences.

4.2.1. Uncertainties in the inferences of M_s and SFR

The SPS models used to fit observational data and infer hence M_s of galaxies are flawed mainly by uncertainties in stellar evolution (for example in the thermally-pulsating asymptotic giant branch, TP-AGB, and horizontal branch phases) and by the poor knowledge of the initial mass function, IMF, as well as due to degeneracies like the one between age and metallicity (see for recent extensive discussions Maraston et al. 2006; Bruzual 2007; Tonini et al. 2009; Conroy, Gunn & White 2009; Santini et al. 2009; Salimbeni et al. 2009). For example, Conroy et al. (2009) estimated that including uncertainties in stellar evolution, M_s at $z \sim 0$ carry errors of ~ 0.3 dex at 95% confidence level with little dependence on luminosity or color.

Maraston et al. (2006) showed that the stellar masses of galaxies with dominating stellar populations of ~ 1 Gyr age could be on average 60% lower if their assumptions for convective overshooting during the TP-AGB phases are used. More recently, Salimbeni et al. (2009) have determined the stellar masses of galaxies from a GOODS-MUSIC sample at redshifts $0.4 < z < 4.0$ by using the Bruzual & Charlot (2003, BC03) and Charlot & Bruzual 2007 (CB07, see Bruzual 2007) SPS models, and the Maraston (2005) models (M05). Salimbeni et al. (2009) have found that the masses obtained with MR05 and CB07 (which take into account the TP-AGB phase) are on average lower than those obtained with BC03. In the redshift bin $0.4 < z < 0.8$ the ratio they have found between BC03 and BC07 masses is ~ 0.3 dex for $M_s < 10^{9.5} M_\odot$ and ~ 0.05 dex for $M_s > 10^{11} M_\odot$, while between BC03 and M05 the ratio is ~ 0.2 dex for all masses.

All the SSFR- M_s relations compiled here and showed in Fig. 5 were inferred using the old BC03 SPS models. If we assume a conservative correction due to the TP-AGB phase of 0.2 dex in M_s for all the masses and a slope of -0.5 in the $\log \text{SSFR} - \log M_s$ relation (in most cases this slope is shallower), then such a relation shifts on average by 0.1 dex ($\approx 25\%$) towards the high-SSFR side. Therefore, if any, the differences between observed and predicted SSFR- M_s relations could be even larger than showed in Fig. 5.

Regarding the determination of SFR, it could significantly depend on the used indicator. For example, in Gilbank et al. (2011) is showed that the SFRs inferred for a sample of galaxies at $z \sim 1$ by using as a indicator the [OII] empirically corrected for extinction as a function of M_s (Gilbank et al. 2010) are on average 2.2 times lower than those inferred by using [OII] + $24\mu\text{m}$, where the [OII] has not been corrected for extinction (since the light from SF being reprocessed by dust should now be measured by the $24\mu\text{m}$ flux). This explains the difference seen in Fig. 5, third panel, in between Gilbank et al. (2011) and Noeske et al. (2007b) (and probably the other authors).

Different indicators have different sensitivities to unobscured/obscured SF. Because observations are required at different z and for different mass and galaxy type ranges, different indicators in the same sample are often used. This unavoidably introduces systematics that difficult the interpretation of correlations and evolutive trends. It should be said that in several of the works compiled here, the combination of two or more indicators that trace both obscured/unobscured SFR were used with calibrations given by SPS models. These calibrations seem to be robust to variations in the stellar evolution and extinction assumptions, but they vary among different assumption on IMF by $\approx 0.1 - 0.4$ dex. The latter systematic variations are partially compensated when calculating the SSFR because both the SFR calibrators and the estimated M_s change in the same direction with varying the IMF. Besides, the effects of extinction are actually minimal at low masses.

In the compilation of observational determinations showed in Fig. 5, a large diversity of SFR indicators, extinction corrections, and galaxy samples were used. Although there are differences in the results among these works, our conclusions do not change when using one or another particular work. This means that among all the current observational determinations, there is a rough convergence regarding the SSFR- M_s relation and its evolution.

4.2.2. Selection effects

Other significant sources of uncertainty and possible systematics in the inferred SSFR– M_s relations at different z are (e.g., Daddi et al. 2007; Chen et al. 2009; Stringer et al. 2010): selection effects due to sample incompleteness in a given wavelength; environmental effects; limit detections of the indicators of SFR due to flux–limits or low emission-line signal-to-noise ratios; in addition, obscured AGN emission could contaminate the infrared flux and some of the optical lines used to estimate SFR, though at low masses AGNs it is not frequent. In most of the works presented here, the authors sought to refine their samples to minimize the above selection effects and the contamination by AGNs.

The main concern among the mentioned above issues is that selection and environmental effects could bias the observed SSFR– M_s relations. For example, the high SSFRs of low-mass galaxies could be due to transient star bursts if the SF regime of these galaxies is dominated by episodic processes. If among the low-mass galaxies those with low SFRs are missed due to detection limits, then the SSFRs of low-mass galaxies will be biased on average toward higher SSFRs, a bias that increases for samples at higher redshifts. Nevertheless, in most of the observational studies reporting the SSFR– M_s relation, the authors discuss that while this is possible at some level, it would hardly change the tight SSFR– M_s relations observed since $z \sim 1$ (see e.g., Noeske et al. 2007a).

On the other hand, the analysis of very local surveys helps to disentangle whether episodic star bursting events dominate or not the SF history of low-mass galaxies⁹. From a study of the SF activity of galaxies within the 11 Mpc Local Volume, Lee et al. (2007; see also Bothwell, Kennicutt & Lee 2009) have found that intermediate–luminosity disc galaxies ($-19 \lesssim M_B \lesssim -15$ or $50 \lesssim V_{\max}/\text{km s}^{-1} \lesssim 120$) show relatively low scatter in their SF activity, implying factors not larger than 2–3 fluctuations in their SFRs; above $V_{\max} \approx 120$ km/s the sequence turns off toward lower levels of SSFRs and larger bulge–to–disc ratios. These results are for nearby galaxies, where selection effects are minimal, and imply that the SSFRs of disc galaxies with $M_s \gtrsim 5 \cdot 10^8 M_\odot$ follow a relatively tight sequence, without strong fluctuations. For galaxies smaller than $V_{\max} \sim 50$ km/s (dwarfs) the situation seems different. The results by Lee et al. (2007) show that a significant fraction of such galaxies are undergoing strong episodic SF fluctuations due to the large scatter in their SSFRs.

Another observational study of nearby galaxies by James et al. (2008), also concluded that there is little evidence in their sample of predominantly isolated field galaxies of significant SF through brief but intense star-burst phases. Therefore, it seems that the tight sequence found for normal star-forming galaxies in the SSFR– M_s plane in large surveys as SDSS (Brinchman et al. 2004; Salim et al. 2007; Schiminovich et al. 2007) is intrinsic and due to a high degree of temporal self-regulated SF within individual galaxies. This sequence (called the ‘main sequence’ in Noeske et al. 2007a) seems to persist back to $z \sim 1$ as discussed above.

Finally, possible selection biases in the SSFR– M_s relation at low masses due to environment seem not to be a concern. For local SDSS and high z (up to $z \sim 1$) zCOSMOS galaxy samples it was found that the relationship between SSFR and M_s is nearly the same in the highest and lowest density quartiles of *star-forming* galaxies (Peng et al. 2010). What is strongly dependent on environment are the fractions of star-

forming and quenched galaxies: the higher the environmental density, the higher the fraction of quenched (red) galaxies, even at lower mass. On the average –where most galaxies live– and low density environments, the fraction of red galaxies becomes smaller and smaller as the masses are lower (Peng et al. 2010). Similar results were found by McGee et al. (2010), who determined stellar masses and SFRs for large samples of field and group galaxies at $z \sim 0$ by using SDDS and at $z \sim 0.4$ by using the Galaxy Environment Evolution Collaboration survey. The SSFR– M_s relation of star-forming galaxies is consistent within the errors in the field and group environment at fixed z , but the fraction of passive (red) galaxies is larger in groups than in the field at almost all masses.

4.2.3. Concluding remarks

We conclude that, in spite of significant uncertainties and possible systematics due to selection effects, current observational determinations of the SSFR– M_s relation for field galaxies at redshifts up to $z \sim 1$ have achieved a rough consistency among them. The global empirical picture of the M_s assembly that they suggest, for sub- M^* central galaxies, begins to be established; however, several important details such as, the separation by galaxy types and environment, are still highly uncertain. According to those works, where the samples were separated into blue/star-forming, red/quenched and/or AGN-dominated galaxies (e.g., Salim et al. 2007; Bell et al. 2007; Noeske et al. 2007a; Karim et al. 2011), the low-mass side of the SSFR– M_s relation is actually dominated by blue/star-forming galaxies, which correspond typically to disk-dominated galaxies.

Big efforts should be done in the next years to determine with better accuracy and completeness the M_s and SFR of galaxies down to small masses, up to high redshifts, and separated by galaxy type and environment. This implies not only observational efforts but also theoretical ones: SPS models, used to infer the physical quantities from the flux and spectroscopy measurements, need to be improved. The information provided by the SSFR as a function of M_s , at different epochs, offers important clues for understanding how galaxies assembled their masses and helps to constrain any theoretical approach to galaxy formation and evolution.

5. CONCLUSIONS

The N-body + Hydrodynamic ART code has been used to simulate sub- M^* central galaxies in the halo mass range of $M_h(z=0) \sim 2 - 40 \times 10^{10} M_\odot$, varying the resolution and several of the sub-grid parameters. Most of the obtained galaxies in our highest resolution simulations have dynamical and structural properties in reasonable agreement with local sub- M^* field galaxies, which typically are disk, late-type galaxies (Figs. 2 and 3, and Table 2).

Although we have simulated only 10 different galaxies, all immersed in different *distinct* halos, our results allows us to answer, at least preliminary, the main questions stated in the Introduction and hence conclude that:

- The SSFRs at $z \sim 0$ and ~ 0.3 of simulated galaxies in the mass range $M_s \sim 10^8 - 10^{10} M_\odot$ are 5 – 10 times lower than the mean values inferred from several observational samples of field galaxies (Fig. 5). There is not a high-resolution simulation with a SSFR value high enough to lie above the lower 1σ scatter of the observational determinations by Salim et al. (2007) of star-forming galaxies at $z \sim 0$ (most observed low-mass

⁹ Have in mind that blue, late-type galaxies are the dominant population in the mass range $10^9 \lesssim M_s/M_\odot \lesssim 5 \cdot 10^{10} M_\odot$ (e.g. Yang et al. 2009).

central galaxies are actually star-forming). At higher redshifts, $z \sim 1.0 - 1.5$, most simulated galaxies have masses below the completeness limits of current observational inferences at those z . However, both the measurements of the SSFRs of those galaxies which are below these limits and the extrapolations to lower masses of the SSFR– M_s relations of the complete samples, are higher than the SSFRs of our simulated galaxies, though the differences are apparently smaller than at $z \sim 0$. Several of the simulations at $z \sim 1.0 - 1.5$ have already SSFRs around the value corresponding to a galaxy forming stars with a rate equal to its past average. On the contrary, at $z \lesssim 0.3$, most simulations have SFR values well below this case, in clear disagreement with most current observational determinations.

- The evolution of the observationally determined SSFR– M_s relations shows a clear trend of downsizing for the typical stellar mass, M_{quench} , of galaxies that transit from active to passive (those that cross below the line of constant SFR at a given z in Fig. 5). There is not any evidence of such a downsizing trend in the simulations.
- The stellar mass fractions ($F_s \equiv M_s/M_h$) of simulated galaxies are 5–10 times larger at $z \sim 0$ than current determinations (semi-empirical and direct) of these fractions as a function of M_s (Fig. 6). At higher redshifts, the differences, at a given mass, increase even more; at $z = 1.5$, the F_s of simulated galaxies are around 30 times larger than the semi-empirical inferences or their extrapolations to lower masses. Put in another way, while the F_s – M_h relation of simulated galaxies would tend to remain constant or slightly shift to higher F_s values as z increases, the current semi-empirical inferences show that the low-mass side of this relation shifts significantly to lower F_s values (see also Fig. 7).

Therefore, our numerical simulations confirm the issues previously found with semi-numerical models of disk galaxy evolution (and eventually SAMs) in the context of the Λ CDM

scenario: *low-mass disk-like galaxy models seem to assemble their stellar masses on average much earlier than suggested by several pieces of evidence such as the observationally inferred SSFR– M_s and F_s – M_s relations at redshifts $z < 1$.* As pointed out in Firmani et al. (2010) and FA10, the M_s assembly of low-mass modeled galaxies follow, in first instance, the mass assembly of their corresponding halos, and in the Λ CDM scenario, low-mass halos assemble on average earlier than more massive halos (upsizing). The different astrophysical processes followed in current models and numerical simulations of galaxy formation and evolution (gas cooling and infall, SF, SF feedback, SN-driven galaxy outflows, etc.) makes the growth of M_s deviates from that of the corresponding dark halo but not as strongly as observations apparently suggest (downsizing; see Fig. 4 in FA10 for a comparison of the average trends of halo MAHs and empirically inferred average galaxy M_s tracks).

If the empirical picture of sub- M^* central galaxies assembly is confirmed (see §4.2 for a discussion in current uncertainties), then the M_s growth of central galaxies less massive than $M_s(z=0) \sim 3 \times 10^{10} M_\odot$ seems to require a significant delay with respect to the evolution of their corresponding Λ CDM halos; besides, the smaller the galaxy the longer such a delay (see also Noeske et al. 2007b). According to Bouché et al. (2010), this mass-dependent delay in the M_s assembly can be explained by a halo mass floor $M_{\text{min}} \approx 10^{11} M_\odot$, below which the halo-driven gas accretion is quenched.

ACKNOWLEDGMENTS

We thank the Referee for his/her comments and suggestions that improved the presentation of the paper. We are grateful to A. Kravtsov for providing us with the numerical code and to N. Gnedin for providing us the analysis and graphics package IFRIT. The authors acknowledge PAPIIT-UNAM grants IN114509 to V.A. and IN112806 to P.C. and CONACyT grant 60354 (to V.A., P.C. and O.V.). Some of the simulations presented in this paper were performed on the HP CP 4000 cluster (Kan-Balam) at DGSCA-UNAM.

APPENDIX

THE COMPILATION OF OBSERVATIONAL WORKS

In Fig. 5 the simulation results in the SSFR– M_s plane are compared with a large body of observational inferences at four z bins compiled from the literature. Following, a brief description of these inferences at each z bin is presented.

a) $z = 0$ panel: The linear fit to the SSFR– M_s relation and its intrinsic width as determined in Salim et al. (2007) for the subsample of normal star-forming galaxies (optical emission lines are used for classifying galaxies) in a volume-corrected sample of around 50,000 SDSS galaxies are shown. The dust-corrected SFRs were obtained by fitting (GALEX) UV and SDSS photometry to a library of dust-attenuated SPS models. While the fraction of galaxies with negligible H α emission-line detection in their sample is significant, most of them are luminous (massive) ones. Therefore, their SSFR– M_s relation for ‘star-forming galaxies’ at low masses ($M_s \lesssim 2 \times 10^{10} M_\odot$) is almost the same if galaxies with no H α detection are included (compare the mentioned fit with the one carried out by the same authors for the *entire* sample, where a Schechter function was used for the fitting, long-dashed line; the characteristic mass is $M_0 = 10^{11.03} M_\odot$). Results similar to Salim et al. (2007) were found by other authors (e.g., Schiminovich et al. 2007).

b) $z = 0.33$ and $z = 1.00$ panels: The median and standard deviation of $\log \text{SSFR}$ vs $\log M_s$ of the sequence of star-forming field galaxies as reported in Noeske et al. (2007b) are plotted in these panels (crosses with vertical error bars). The data used by these authors consisted of 2905 galaxies out to $z = 1.1$ from the All-Wavelength Extended Groth Strip International Survey (AEGIS). The SFRs for galaxies with robust 24 μm detections were derived from 24 μm luminosity + non-extinction corrected emission lines, and for galaxies below the 24 μm detection, from extinction-corrected emission lines. The symbols show only the M_s range where the sample is $> 95\%$ complete in the redshift bins $0.20 \leq z < 0.45$ and $0.85 \leq z < 1.10$, respectively. For masses smaller than the sample completeness ($M_s \sim 10^8 M_\odot$ and $\sim 10^9 M_\odot$, respectively) the derived SSFRs continue to increase on average for lower values of M_s . Around 30% of galaxies in their sample at all z have not robust 24 μm or emission-line detections, which implies very low SFRs. The inclusion of these galaxies in the SSFR– M_s relation, decreases the overall median SSFRs and it would be lower than the one shown in Fig. 5. However, almost all of these galaxies ($> 90\%$) are in the red

TABLE A1
SUMMARY OF SOURCES AND CORRECTIONS

Source	SFR tracer	IMF	M_s offset ^a	SFR offset ^b
Salim et al. (2007)	L_{UV}, H_α	Chabrier (2003)	0.0	0.0
Bell et al. (2007)	$L_{IR} + L_{UV}$	Chabrier (2003)	0.0	0.0
Noeske et al. (2007)	$L_{24\mu m} + \text{emission lines}$	Kroupa (2001)	0.0	0.0
Santini et al. (2009)	$L_{IR} + L_{UV}$	Salpeter (1955)	-0.25	-0.176
Damen et al. (2009)	$L_{IR} + L_{UV}$	Kroupa (2001)	0.0	0.0
Dunne et al. (2009)	$L_{1400MHz}$	Salpeter (1955)	-0.25	-0.176
Kajisawa et al. (2010)	$L_{UV}(\text{corrected})$	Salpeter (1955)	-0.25	-0.176
Karim et al. (2010)	$L_{1400MHz}$	Chabrier (2003)	0.0	0.0
Rodighiero et al. (2010)	$L_{IR} + L_{UV}$	Salpeter (1955)	-0.25	-0.176
Gilbank et al. (2011)	$[OII]-(H_\alpha)$	Baldry & Glazebrook (2003)	-0.08	-0.18

^aShift in dex to convert M_s to the Chabrier IMF

^bShift in dex to convert SFR to the Chabrier IMF

sequence and have early-type morphologies, being besides relatively massive (Noeske et al. 2007a; Noeske et al. 2007b).

In these panels are also plotted the average data (from stacking) taken from the SSFR vs M_s plots at $0.2 < z \leq 0.4$ and $0.8 < z \leq 1.0$ given in Bell et al. (2007) for ‘all galaxies’ (open stars) and for blue galaxies only (blue asterisks). Results correspond to the Chandra Deep Field South (CDFS) sample; the COMBO-17 survey in conjunction with *Spitzer* 24 μm data were used for estimating M_s and SFR (for the latter, UV and 24 μm luminosities were used). In the low-mass side ($M_s < 3 \cdot 10^{10} M_\odot$) and for all z bins, blue galaxies dominate in such a way that the average SSFRs for the total sample (blue + red galaxies) is close to the average of the blue cloud sample. The mass completeness limits reported in Bell et al. (2007) are indicated with the dotted vertical arrows.

c) $z = 0.33$, $z = 1.00$, and $z = 1.50$ panels: Santini et al. (2009) presented least-square linear fits to the SFR– M_s relations ($\text{SFR} = A M_s^\beta$) obtained from the GOOD-MUSIC catalog, which has multi-wavelength coverage from 0.3 to 24 μm (complete SED fittings and UV–24 μm luminosities were used for estimating SFRs). We plot in Fig. 5 these fits but divided by M_s (blue lines) for the redshift intervals $0.3 \leq z < 0.6$ (second panel), $0.6 \leq z < 1.0$ and $1.0 \leq z < 1.5$ (third panel), and $1.0 \leq z < 1.5$ and $1.5 \leq z < 2.5$ (fourth panel).

Similarly, the fits to the SSFR– M_s relations obtained in Rodighiero et al. (2010) for the redshift bins $0.3 \leq z < 0.6$ (second panel), $0.6 \leq z < 1.0$ and $1.0 \leq z < 1.5$ (third panel), and $1.0 \leq z < 1.5$ and $1.5 \leq z < 2.5$ (fourth panel) are plotted (black solid lines). These authors used deep observations of the GOODS-N field taken with PACS on board of the *Herschel* satellite, which allows them to robustly derive the total infrared luminosity of galaxies, and combine with the ancillary UV luminosities in order to calculate the SFRs. In both cases Santini et al. (2009) and Rodighiero et al. (2010), we plot their fits only for masses where samples are complete.

The linear fits to radio–stacking-based measurements of the SSFR as a function of M_s recently presented by Karim et al. (2011) are also plotted in these three panels (long-dashed red line). The fits correspond to star-forming galaxies from a deep 3.6– μm –selected sample of $> 10^5$ galaxies ($0.2 < z < 3$) in the 2 deg² COSMOS field, and are shown only for galaxies above the completeness limit at the given z . The fits to the entire sample are steeper than those to only star-forming galaxies, in such a way that at low masses both intersect, but at larger masses, the former lie below the latter. The image-stacking technique applied in order to increase the signal-to-noise ratio in the VLA 1.4 GHz radio continuum observations allows one to estimate only average SFRs of the stacked population; they cannot shed light on the intrinsic dispersion of individual sources.

Also shown in these panels are the average SSFRs corresponding to the lowest mass bins –where given samples are still complete– from:

Damen et al. (2009b).– The mass bins of 0.5 dex width in each panel correspond to $z \approx 0.4, 1.0$ and 1.4 , respectively; the horizontal error bar indicates the width of the M_s bin, 0.5 dex, and the vertical error bar represents the bootstrapped 68% confidence level on the average SSFR in the bin; the FIREWORKS catalog for the GOODS-CDFS generated by Wuyts et al. (2008) was used to infer M_s and SFRs (infrared and UV luminosities were combined to derive the latter and no selection on color/morphology was applied; i.e., all galaxies were included).

Dunne et al. (2009).– The lowest complete mass bins of 1 dex width correspond to $z = 0.50, 0.95$, and 1.40 , respectively, with the average SSFRs and their scatters shown with the error bars centered in the median value of the mass bin; stacked deep radio mosaics of K –band selected galaxies from the UKIDSS were used to determine M_s and SFRs –rest-frame 1400-MHz luminosities were used to derive the latter; the case using the Bell et al. (2003) conversion and applied to the whole sample is reproduced here.

Kajisawa et al. (2010).– The lowest complete mass bins of 0.5 dex width correspond to the median dust-corrected SFRs, where the rest-frame 2800 Å luminosity was used as indicator. This UV luminosity was estimated by the best-SED fitting of the multi-band photometry ($UBVizJHK$, 3.6 μm , 4.5 μm , and 5.8 μm) with the BC03 models. We reproduce the reported values at redshift bins of $0.5 < z < 1.0$, and $1.0 < z < 1.5$.

After the completion of this paper, appeared the work by Gilbank et al. (2011), where the SSFR– M_s relation for star-forming galaxies at $z \sim 1$ is presented down to masses smaller than those previously determined (their linear fit is plotted in panel $z = 1$ of Fig. 5 with a long-dashed purple line). For the low-mass side, they analyzed a sample of 199 low-mass galaxies ($10^{8.5} \lesssim M_s/M_\odot \lesssim 10^{9.3}$) from the field CDFS, with spectroscopy redshifts determined in the range $0.88 < z \leq 1.15$ and a

sampling completeness $> 80\%$ (Gilbank et al. 2010). Stellar masses were determined by SED-fitting of the photometry, at the given z , using a grid of PEGASE.2 models. The [OII] line is used as the SFR indicator (actually the Kennicutt 1998 SFR– $H\alpha$ relation is used by assuming an [OII]/ $H\alpha$ ratio of 0.5), empirically corrected as a function of M_s in order to correct for extinction and other systematic effects. Their correction implies on average a lower SFR than previously determined, by using for example [OII](non-corrected) + $24\mu\text{m}$ (see for a discussion §4.2.1). The relation by Gilbank et al. (2011) is indeed the one that implies the lowest estimates for SSFR among all those compiled in Fig. 5 at $z \approx 1$. These authors estimated also the local SSFR– M_s of blue galaxies by using SDSS Stripe 82 and the $H\alpha$ line as the SFR indicator. The linear fit to their results lies below the average relation reported by Salim et al. (2007, by ≈ 0.25 dex at $10^9 M_\odot$).

In Table A1, a summary of all the sources used in Fig. 5 and described above is presented. In all the cases, $h = 0.70$ or 0.71 was assumed. Columns 2 and 3 report the main SFR indicator(s) and IMF used in each source, respectively. Columns 4 and 5 give the average shifts in dex applied here respectively to M_s and SFR in order to correct for a Chabrier (2003) IMF when necessary. According to Bell et al. (2007), the stellar masses and SFRs calculated with Chabrier (2003) and Kroupa (2001) IMFs (when using $L_{IR} + L_{UV}$ as indicator) are consistent to within $\lesssim 10\%$, so we do not apply corrections for those cases when a Kroupa (2001) IMF was used (see for similar conclusions Karim et al. 2010 and Salim et al. 2007 for the $L_{1400\text{MHz}}$ and $H\alpha$ indicators, respectively). For the corrections in cases when the (Salpeter 1955) IMF was used, see Santini et al. (2009). For the Baldry & Glazebrook (2003) IMF, we have used the corrections given in Gilbank et al. (2011) for passing to a Kroupa (2001) IMF. We are aware that all these corrections are yet uncertain, and could actually vary from indicator to indicator and with z . In any case, they are relatively small, in particular for the SSFR.

REFERENCES

- Agertz, O., Teyssier, R., & Moore, B. 2011, MNRAS, 410, 1391
 Avila-Reese, V., Zavala, J., Firmani, C., & Hernández-Toledo, H. M. 2008, AJ, 136, 1340
 Baldry, I. K., & Glazebrook, K. 2003, ApJ, 593, 258
 Baldry, I. K., Glazebrook, K., Brinkmann, J., Ivezić, Ž., Lupton, R. H., Nichol, R. C., & Szalay, A. S. 2004, ApJ, 600, 681
 Bauer, A. E., Drory, N., Hill, G. J., & Feulner, G. 2005, ApJL, 621, L89
 Behroozi, P. S., Conroy, C., & Wechsler, R. H. 2010, ApJ, 717, 379
 Bekki, K. 2008, ApJL, 680, L29
 Bell, E. F., McIntosh, D. H., Katz, N., & Weinberg, M. D. 2003, ApJL, 585, L117
 Bell, E. F., Zheng, X. Z., Papovich, C., Borch, A., Wolf, C., Meisenheimer, K., 2007, ApJ, 663, 834
 Benson, A. J., Bower, R. G., Frenk, C. S., Lacey, C. G., Baugh, C. M., & Cole, S. 2003, ApJ, 599, 38
 Bertone, S., De Lucia, G., & Thomas, P. A. 2007, MNRAS, 379, 1143
 Bothwell, M. S., Kennicutt, R. C., & Lee, J. C. 2009, MNRAS, 400, 154
 Bouché, N., et al. 2010, ApJ, 718, 1001
 Bower, R. G., Benson, A. J., Malbon, R., Helly, J. C., Frenk, C. S., Baugh, C. M., Cole, S., & Lacey, C. G. 2006, MNRAS, 370, 645
 Brinchmann, J., Charlot, S., White, S. D. M., Tremonti, C., Kauffmann, G., Heckman, T., & Brinkmann, J. 2004, MNRAS, 351, 1151
 Brooks, A., et al. 2011, ApJ, 728, 51
 Bruzual, G., & Charlot, S. 2003, MNRAS, 344, 1000
 Bruzual, G. 2007, From Stars to Galaxies: Building the Pieces to Build Up the Universe, in "Astronomical Society of the Pacific Conference Series", Eds. A. Vallenari, R. Tantaló, L. Portinari, & A. Moretti, 374, 303
 Bundy, K., et al. 2006, ApJ, 651, 120
 Ceverino, D., & Klypin, A. 2009, ApJ, 695, 292
 Chabrier, G. 2003, PASP, 115, 763
 Chen Y.-M., Wild V., Kauffmann G., Blaizot J., Davis M., Noeske K., Wang J.-M., Willmer C., 2009, MNRAS, 393, 406
 Colín, P., Avila-Reese, V., Vázquez-Semadeni, E., Valenzuela, O., & Ceverino, D. 2010, ApJ, 713, 535
 Conroy, C., Gunn, J. E., & White, M. 2009, ApJ, 699, 486
 Conroy, C., & Wechsler, R. H. 2009, ApJ, 696, 620
 Cowie, L. L., Songaila, A., Hu, E. M., Cohen, J. G., 1996, AJ, 112, 839
 Croton, D. J., et al. 2006, MNRAS, 367, 864
 Daddi, E., et al. 2007, ApJ, 670, 173
 Damen, M., Labbé, I., Franx, M., van Dokkum, P. G., Taylor, E. N., & Gawiser, E. J. 2009a, ApJ, 690, 937
 Damen, M., Förster Schreiber, N. M., Franx, M., Labbé, I., Toft, S., van Dokkum, P. G., & Wuyts, S. 2009b, ApJ, 705, 617
 De Lucia, G., Kauffmann, G., & White, S. D. M. 2004, MNRAS, 349, 1101
 De Lucia, G., Springel, V., White, S. D. M., Croton, D., & Kauffmann, G. 2006, MNRAS, 366, 499
 De Rijcke, S., Zeilinger, W. W., Hau, G. K. T., Prugniel, P., & Dejonghe, H. 2007, ApJ, 659, 1172
 de Rossi, M. E., Tissera, P. B., & Pedrosa, S. E. 2010, A&A, 519, A89
 Drory, N., & Alvarez, M. 2008, ApJ, 680, 41
 Drory, N., et al. 2009, ApJ, 707, 1595
 Dunne, L., et al. 2009, MNRAS, 394, 3
 Dutton, A. A., & van den Bosch, F. C. 2009, MNRAS, 396, 141
 Dutton, A. A., van den Bosch, F. C., & Dekel, A. 2010a, MNRAS, 405, 1690
 Dutton, A. A., et al. 2010b, MNRAS, 405, 1693
 Elbaz, D., et al. 2007, A&A, 468, 33
 Fakhouri, O., Ma, C.-P., & Boylan-Kolchin, M. 2010, MNRAS, 406, 2267
 Ferland, G. J., Korista, K. T., Verner, D. A., Ferguson, J. W., Kingdon, J. B., & Verner, E. M. 1998, PASP, 110, 761
 Feulner, G., Gabasch, A., Salvato, M., Drory, N., Hopp, U., & Bender, R. 2005, ApJL, 633, L9
 Firmani, C., & Avila-Reese, V. 2000, MNRAS, 315, 457
 Firmani, C., & Avila-Reese, V. 2010, ApJ, 723, 755 (FA10)
 Firmani, C., Avila-Reese, V., & Rodríguez-Puebla, A. 2010, MNRAS, 404, 1100
 Fontanot, F., De Lucia, G., Monaco, P., Somerville, R. S., & Santini, P. 2009, preprint (astro-ph/0901.1130)
 Geha, M., Blanton, M. R., Masjedi, M., & West, A. A. 2006, ApJ, 653, 240
 Gibson, B. K., Courty, S., Sánchez-Blázquez, P., Teyssier, R., House, E. L., Brook, C. B., & Kawata, D. 2009, IAU Symposium, 254, 445
 Gilbank, D. G., et al. 2011, MNRAS, 402, in press, arXiv:1101.3780
 Gilbank, D. G., et al. 2010, MNRAS, 405, 2419
 Governato, F., Willman, B., Mayer, L., Brooks, A., Stinson, G., Valenzuela, O., Wadsley, J., & Quinn, T. 2007, MNRAS, 374, 1479
 Governato, F., et al. 2010, Nature, 463, 203
 Guo, Q., & White, S. D. M. 2008, MNRAS, 384, 2
 Guo, Q., White, S., Li, C., & Boylan-Kolchin, M. 2010, MNRAS, 404, 1111
 Haardt, F., & Madau, P. 1996, ApJ, 461, 20
 Hopkins, P. F., Bundy, K., Hernquist, L., & Ellis, R. S. 2007, ApJ, 659, 976
 James, P. A., Prescott, M., & Baldry, I. K. 2008, A&A, 484, 703
 Kajisawa, M., et al. 2009, ApJ, 702, 1393
 Kajisawa, M., Ichikawa, T., Yamada, T., Uchimoto, Y. K., Yoshikawa, T., Akiyama, M., & Onodera, M. 2010, ApJ, 723, 129
 Karim, A., et al. 2011, ApJ, 730, 61
 Kennicutt, R. C., Jr. 1998, ARA&A, 36, 189
 Kereš, D., Katz, N., Davé, R., Fardal, M., & Weinberg, D. H. 2009, MNRAS, 396, 2332
 Klypin, A., & Holtzman, J. 1997, preprint (astro-ph/9712217)
 Klypin, A., Kravtsov, A. V., Bullock, J. S., & Primack, J. R. 2001, ApJ, 554, 903
 Klypin, A., Trujillo-Gomez, S., & Primack, J. 2010, arXiv:1002.3660
 Kravtsov, A. V., Klypin, A. A., & Khokhlov, A. M., 1997, ApJSS, 111, 73
 Kravtsov, A. V. 2003, ApJL, 590, L1
 Kravtsov, A. V., Nagai, D., & Vikhlinin, A. A. 2005, ApJ, 625, 588
 Kroupa, P. 2001, MNRAS, 322, 231
 Lee, J. C., Kennicutt, R. C., Funes, S. J., José, G., Sakai, S., & Akiyama, S. 2007, ApJL, 671, L113
 Li, Y., Mo, H. J., & Gao, L. 2008, MNRAS, 389, 1419
 Liu, L., Yang, X., Mo, H. J., van den Bosch, F. C., & Springel, V. 2010, ApJ, 712, 734
 Maraston, C. 2005, MNRAS, 362, 799
 Maraston C., Daddi E., Renzini A., Cimatti A., Dickinson M., Papovich C., Pasquali A., Pirzkal N., 2006, ApJ, 652, 85
 Martig, M., Bournaud, F., Teyssier, R., & Dekel, A. 2009, ApJ, 707, 250
 Mayer, L., Governato, F., & Kaufmann, T. 2008, Advanced Science Letters, 1, 7
 Miller, G. E., & Scalo, J. M. 1979, ApJSS, 41, 513
 McGaugh, S. S. 2005, ApJ, 632, 859
 McGee, S. L., Balogh, M. L., Wilman, D. J., Bower, R. G., Mulchaey, J. S., Parker, L. C., & Oemler, A., Jr. 2010, MNRAS, in press, arXiv:1012.2388
 More, S., van den Bosch, F. C., Cacciato, M., Skibba, R., Mo, H. J., & Yang, X. 2010, MNRAS, 406, 1464
 Mortlock, A., Conselice, C. J., Bluck, A. F. L., Bauer, A. E., Gruetzbauch, R., Buitrago, F., & Ownsworth, J. 2011, MNRAS, in press, arXiv:1101.2867
 Moster, B. P., Somerville, R. S., Maudsells, C., van den Bosch, F. C., Maccio, A. V., Naab, T., & Oser, L. 2010, ApJ, 710, 903
 Naab, T., Johansson, P. H., Ostriker, J. P., & Efstathiou, G. 2007, ApJ, 658, 710
 Neistein, E., van den Bosch, F. C., & Dekel, A. 2006, MNRAS, 372, 933
 Noeske, K. G., et al. 2007a, ApJL, 660, L43

- Noeske K. G., et al. 2007b, *ApJ*, 660, L47
- Oliver, S., et al. 2010, *MNRAS*, 405, 2279
- Oppenheimer, B. D., & Davé, R. 2008, *MNRAS*, 387, 577
- Oppenheimer, B. D., Davé, R., Kereš, D., Fardal, M., Katz, N., Kollmeier, J. A., & Weinberg, D. H. 2010, *MNRAS*, 406, 2325
- Pasquali, A., Gallazzi, A., Fontanot, F., van den Bosch, F. C., De Lucia, G., Mo, H. J., & Yang, X. 2010, *MNRAS*, 407, 937
- Peng, Y., et al. 2010, *ApJ*, 721, 193
- Piontek, F., & Steinmetz, M. 2011, *MNRAS*, 410, 2625
- Pozzetti, L., et al. 2010, *A&A*, 523, A13
- Rodighiero, G., et al. 2010, *A&A*, 518, L25
- Rodríguez-Puebla, A., Avila-Reese, V., Firmani, C., & Colín, P. 2010, *RevMexAA*, 48, in press, arXiv:1103.4151
- Saitoh, T. R., Daisaka, H., Kokubo, E., Makino, J., Okamoto, T., Tomisaka, K., Wada, K., & Yoshida, N. 2008, *PASJ*, 60, 667
- Salim S., et al., 2007, *ApJS*, 173, 267
- Salimbeni, S., Fontana, A., Giallongo, E., Grazian, A., Menci, N., Pentericci, L., & Santini, P. 2009, *American Institute of Physics Conference Series*, 1111, 207
- Salpeter, E. E. 1955, *ApJ*, 121, 161
- Santini, P., et al. 2009, *A&A*, 504, 751
- Sawala, T., Guo, Q., Scannapieco, C., Jenkins, A., & White, S. D. M. 2011, *MNRAS*, 64
- Scannapieco, C., Tissera, P. B., White, S. D. M., & Springel, V. 2006, *MNRAS*, 371, 1125
- Scannapieco, C., Tissera, P. B., White, S. D. M., & Springel, V. 2008, *MNRAS*, 389, 1137
- Schiminovich, D., et al. 2007, *ApJSS*, 173, 315
- Somerville, R. S., et al. 2008, *ApJ*, 672, 776
- Springel, V., White, S. D. M., Tormen, G., & Kauffmann, G. 2001, *MNRAS*, 328, 726
- Stinson, G. S., Dalcanton, J. J., Quinn, T., Gogarten, S. M., Kauffmann, T., & Wadsley, J. 2009, *MNRAS*, 395, 1455
- Stringer, M. J., & Benson, A. J. 2007, *MNRAS*, 382, 641
- Stringer, M., Cole, S., Frenk, C. S., & Stark, D. P. 2011, *MNRAS*, 481
- Tonini, C., Maraston, C., Devriendt, J., Thomas, D., & Silk, J. 2009, *MNRAS*, 396, L36
- Valenzuela, O., Rhee, G., Klypin, A., Governato, F., Stinson, G., Quinn, T., & Wadsley, J., 2007, *ApJ*, 657, 773
- van den Bosch, F. C. 2000, *ApJ*, 530, 177
- Vergani, D., et al. 2008, *A&A*, 487, 89
- Wang, L., & Jing, Y. P. 2010, *MNRAS*, 402, 1796
- Weinmann, S. M., van den Bosch, F. C., & Pasquali, A. 2011, arXiv:1101.3244
- White, S. D. M., & Rees, M. J. 1978, *MNRAS*, 183, 341
- White, S. D. M., & Frenk, C. S. 1991, *ApJ*, 379, 52
- Wuyts, S., Labbé, I., Schreiber, N. M. F., Franx, M., Rudnick, G., Brammer, G. B., & van Dokkum, P. G. 2008, *ApJ*, 682, 985
- Yang, X., Mo, H. J., & van den Bosch, F. C. 2009, *ApJ*, 695, 900
- Zavala, J., Okamoto, T., & Frenk, C. S. 2008, *MNRAS*, 387, 364
- Zheng X. Z., Bell E. F., Papovich C., Wolf C., Meisenheimer K., Rix H.-W., Rieke G. H., Somerville R., 2007, *ApJ*, 661, L41